Tampere University

Timo Stolt

NONLINEAR OPTICS USING RESONANT METAMATERIAL STRUCTURES

Faculty of Engineering and Natural Sciences
Master of Science (Technology) Thesis
November 2019

ABSTRACT

Timo Stolt: Nonlinear optics using resonant metamaterial structures
Master of Science (Technology) Thesis
Tampere University
Science and Engineering
November 2019

Metamaterials are artificial structures consisting of nanoscale building blocks that exhibit properties not found in nature. They have recently shown potential for utilizing nonlinear processes such as second-harmonic generation (SHG) and spontaneous parametric down-conversion (SPDC) in nanoscale applications. Despite the constant progress, metamaterials still lack in terms of conversion efficiency when compared with conventional nonlinear materials that benefit of long propagation lengths and gradual increase of signals via phase matching.

In previous studies of plasmonic metamaterials, the nonlinear properties of metal nanoparticles are enhanced with localized surface plasmon resonances (LSPRs). These resonances have rather short lifetimes leading to high losses typical to metal nanoparticles. Therefore, alternative approaches to realize efficient metamaterials are required.

In this thesis, we present two enhancement methods that are rather well known and studied but not yet fully utilized in nonlinear nanophotonics. The first methods is to utilize collective responses of periodic nanoscale structures known as surface lattice resonances (SLRs) and guided-mode resonances (GMRs). They are associated with narrow spectral features implying the presence of strong local fields and thus enhanced nonlinear responses. Another method to enhance local fields is to couple relevant fields to an external cavity. This method is used in various nonlinear applications such as in optical parametric oscillators (OPOs) and it has been studied also in nanoscale processes.

Here, we investigate how SLRs and microcavities could be used to improve nonlinear metamaterials. First, we perform proof-of-principle studies showing that utilization of GMRs can dramatically enhance SHG occurring in sub-wavelength dielectric gratings. We measure linear and SH response of two silicon nitride gratings and compare the results with simulations based on the nonlinear scattering theory (NLST). As our experiments agree with simulations, we then propose two novel plasmonic metamaterial structures designed for SPDC. The first structure is a metasurface consisting of L-shaped aluminum nanoparticles arranged in a rectangular lattice. The metasurface exhibits SLRs at pump and signal wavelengths resulting in a strong enhancement for the SPDC process where the pump and signal have orthogonal polarizations. Thus, the metasurface mimics a type-I SPDC-crystal which are widely used in quantum optics as photon-pair sources.

Our second design consists of a singly-resonant plasmonic metasurface that is placed inside a microcavity formed with two distributed Bragg reflectors. The cavity is designed to resonate with the pump while the SLR of the metasurface is designed to enhance the local field at the signal wavelength. Our simulations demonstrate a polarization-independent operation where the SPDC is dramatically enhanced at the operation wavelength. This design then can act as either type-0, type-I or type-II nonlinear material, which are all used in quantum optics.

The simulations presented here demonstrate a clear path towards efficient photon-pair generation with nanoscale structures via SPDC. In addition to SHG and SPDC, our structure designs and methods could be utilized also for other nonlinear processes such as cascaded third-harmonic generation or difference-frequency generation. These approaches could pave the path towards development of nanoscale light sources operating in ultraviolet and terahertz regions.

Keywords: nonlinear optics, plasmonics, metasurfaces, surface lattice resonance, optical resonators, distributed Bragg reflectors, nonlinear scattering theory

TIIVISTELMÄ

Timo Stolt: Epälineaarinen optiikka resonanteissa metamateriaaleissa
Diplomityö
Tampereen yliopisto
Teknis-luonnontieteellinen
Marraskuu 2019

Metamateriaalit ovat keinotekoisia rakenteita, joilla on luonnosta löytymättömiä ominaisuuksia. Metamateriaalit koostuvat yleensä nanoskaalan rakenteista kuten metallinanohiukkasista. Viimeaikainen kehitys nanorakenteiden valmistuksessa on mahdollistanut epälineaaristen ilmiöiden, kuten taajuudenkahdennuksen tai parametrisen fluoresenssin (eng. spontaneous parametric down-conversion, SPDC) tutkimisen metamateriaaleissa. Jatkuvasta kehityksestä huolimatta metamateriaalien epälineaariset vasteet ovat huomattavasti heikompia kuin perinteisten epälineaaristen materiaalien, jotka hyödyntävät vaihesovitusmenetelmiä.

Tässä työssä esitellään kaksi menetelmää, joita on tutkittu ja sovellettu laajasti, mutta joiden mahdollisia nanoskaalan sovelluksia on vasta hiljattain alettu tutkimaan. Ensimmäinen menetelmä hyödyntää hilaresonansseja, jotka ovat jaksollisten rakenteiden vasteita. Hilaresonanssien viritystilat ovat tyypillisiä materiaalivasteita huomattavasti pitkäikäisempiä. Tämän seurauksena epälineaariset vasteet voimistuvat niitä käyttämällä paljon enemmän ja paljon kapeammalla kaistanleveydellä, kuin aikaisemissa tutkimuksissa. Toisena menetelmänä käsitellään oleellisten kenttien kytkemistä optisiin resonaattoreihin, joita on jo pitkään hyödynnetty useissa epälineaarisen optiikan sovelluksissa, kuten optisissa parameterisissa oskillaattoreissa.

Tässä työssä tutkitaan kuinka hilaresonanssien ja optisien resonaattoreiden avulla voidaan vahvistaa metamateriaalien epälineaarisia vasteita. Työn ensimmäisessä osassa osoitettiin hilaresonanssien vaikutus mittaamaalla taajuudenkahdennusta resonanteista piinitridihiloista. Mittaustuloksia vertailtiin simulaatiotuloksiin, jotka perustuivat epälineaariseen sirontateoriaan. Mittaukset ja simulaatiot yhtenäisesti osoittivat hilaresonanssien toimivuuden, mikä kannustaa suunnitelemaan uusia metamateriaalirakenteita mainittujen menetelmien avulla.

Työn toisessa osassa esitellään kaksi resonanttia metamateriaalirakennetta, jotka on suunniteltu mahdollisimman tehokkaaseen fotoniparien muodostukseen SPDC:n avulla. Ensimmäisenä materiaalina tutkittiin alumiininanopartikkeleista muodostettua metamateriaalia. Partikkelit asetettiin suorakulmaiseen hilaan siten, että näytteellä oli hilaresonanssit sekä pumppu- että signaaliaallonpituuksilla. Tällöin huomattiin huomattava vahvistus SPDC-vasteessa, kun pumppu ja signaali ovat kohtisuorasti polarisoituneita. Täten metamateriaali voisi toimia fotoniparilähteenä kvanttioptiikan sovelluksissa.

Toinen ehdotettu rakenne koostuu metamateriaalista, joka on asetettu mikroskaalan resonaattoriin. Suurin SPDC:n vahvistus saadtiin kytkemällä pumppu Bragg-hiloista muodostettuun resonaattoriin samalla, kun hilaresonanssit vahvistavat paikalliskenttiä signaaliaallonpituudella. Signaalien arvioitiin olevan yhtä voimakattaita kaikille sallituille polarisaatioyhdistelmille, mikä kuvastaa kyseisen metamateriaalin toiminnan joustavuutta ja soveltuvuutta moniin eri käytttötarkoituksiin.

Työssä esitetyt simulaatiot kannustavat resonanttien metamateriaalien kehittämiseen nanoskaalan fotoniparimuodostusta varten. SPDC:n ja taajuudenkahdennuksen lisäksi työssä esiteltyjä rakenteita voidaan käyttää myös muiden epälineaaristen ilmiöiden kuten taajuudenkolmennuksen tai erotustaajuden muodostuksen vahvistamiseen metamateriaaleissa. Tämän työn tulokset voisivat siten olla lähtökohta tutkimukselle, jonka tavoitteena olisi ultravioletti-ja terahertsialueilla toimivien nanoskaalan valonlähteiden kehittäminen.

Avainsanat: epälineaarinen optiikka, plasmoniikka, hilaresonanssi, metamateriaalit, optinen resonaattori, Bragg-hila, epälineaarinen sirontateoria

PREFACE

This Master of Science Thesis has been conducted in the Photonics Laboratory at Tampere University. Most of the experimental work was done in the spring of 2019, and the simulation work in the Summer and the early autumn of the same year. The work conducted for this Thesis was part of the basic research done in the Nonlinear optics group aiming to improve the nonlinear properties of nanoscale structures.

First, I thank my supervisor Doctor Mikko Huttunen for all his work and for the interesting research topic he has introduced me to. Without his guidance and support, the work done for this Thesis would have not been possible. I thank also Professor Humeyra Caglayan for being the examiner for this Thesis. I also thank Professor Martti Kauranen and Doctor Robert Czaplicki for their guidance in the earlier years of my career as a research assistant. Furthermore, I also thank Professor Tapio Niemi for providing the samples used in the experimental work of this Thesis. For the practical help in the laboratory, I want to thank Doctor Kalle Koskinen for his help with the measurements. I also thank Anna for aiding in the final steps of the simulations. Especially, I want to thank Antti for all his help in the lab over the years.

For the good times in and outside of the lab, I thank Sofia, Martti L, Juha T, Leevi and all the other former and current colleagues and friends in the lab. The warm and welcoming community in the SK1-corridor is something that I have really enjoyed being a part of. I also want to thank Riina, Markus, Tommi, and Jussi for all the good times during my study years. Thanks to their friendship and support, these past five years have been the best time of my life.

Finally, I thank my family: My mother Riitta, my father Tauno and my brother Eero. Your life-long support and care have helped me to become the person I am today.

Tampere, 11th November 2019

Timo Stolt

CONTENTS

LIST OF SYMBOLS AND ABBREVIATIONS

B_0	Amplitude of the magnetic flux
$D(\omega)$	Denominator function
E	Electric field
E_0	Amplitude of the electric field
E_p	Photon energy
$E_{loc}(\omega)$	Local-field coefficient
I	Irradiance
I_0	Fundamental irradiance
I_{SHG}	Second-harmonic generation irradiance
L	Length of an optical resonator
N	Number density of atoms
Q	Quality factor
R	Reflectance
$\Delta\lambda$	Wavelength linewidth
$\Delta\nu_L$	Laser bandwidth
$\Delta\nu_c$	Cavity mode linewidth
$\Delta\nu_{fsr}$	Free spectral range
$\Delta\omega_s$	Gain linewidth of a nonlinear medium
$\Delta\phi$	Round-trip phase shift
$\Delta\theta$	Angular linewidth
$\Delta_{i,j,k}$	Miller's delta
Δk	Wavevector mismatch
Λ	Grating period
$\chi^{(1)}$	Linear susceptibility
$\chi^{(2)}$	Second-order susceptibility
$\chi^{(n)}$	Susceptibility of the nth-order
ϵ_0	Vacuum permittivity
γ	Damping constant
λ	Wavelength
λ_0	Resonance wavelength
λ_B	Bragg wavelength
$\mathbf{k}$	Propagation vector
$\mathbf{p}$	Dipole momentum
$\mathbf{r}$	Position vector
μ_0	Vacuum permeability
ν	Frequency
ω	Angular frequency
ω_0	Resonance frequency
ϕ	Internal phase-shift
ρ_f	Free charge density
τ_c	Photon lifetime
θ	Incident angle
$\mathbf{B}$	Magnetic flux density
$\mathbf{D}$	Electric displacement
$\mathbf{E}$	Electric field vector
$\mathbf{H}$	Magnetic field
$\mathbf{J}_f$	Free current density
$\mathbf{M}$	Magnetization
$\mathbf{P}$	Polarization field
$\mathbf{S}$	Poynting vector
a	Nonlinear parameter of the Lorenz model
$c.c.$	Complex conjugate
c_0	Vacuum speed of light
f	Focal length
h	Planck's constant
k	Propagation number

n	Refractive index
n_{eff}	Effective refractive index
t	Time
DBR	Distributed Bragg reflector
DFG	Difference-frequency generation
FDTD	Finite-difference time-domain
GMR	Guided-mode resonance
HWP	Half-wave plate
LP	Linear polarizer
LPF	Long-pass filter
LSPR	Localized surface plasmon resonance
MNP	Metal nanoparticles
Nd:YAG	Neodymium-doped yttrium aluminum garnet
NLST	Nonlinear scattering theory
OPO	Optical parametric oscillator
PD	Photo diode
RA	Rayleigh anomaly
RWG	Resonant waveguide grating
SFG	Sum-frequency generation
SHG	Second-harmonic generation
SiN	Silicon nitride
SiO_2	Silicon dioxide
SLR	Surface lattice resonance
SPDC	Spontaneous parametric down-conversion
SPF	Short-pass filter
SRC	Singly-resonant-in-cavity
TiO_2	Titanium dioxide

1 INTRODUCTION

Nonlinear optics is a sub-field of physics that studies the interaction between matter and intense light. In nonlinear processes, the material response is no longer linearly dependent on the fundamental field which can lead to the generation of new frequency components. The most studied and well known nonlinear process is called *second-harmonic generation* (SHG) in which the fundamental frequency of a laser is converted to the doubled frequency via three-wave mixing. SHG was first detected by Franken et. al. in 1961 [1] and since then other nonlinear processes have been studied and utilized in different laser applications. One widely used nonlinear process utilized for down-conversion of the fundamental frequency is called *difference-frequency generation* (DFG) which is widely utilized in tunable laser sources operating in ultraviolet, visible and infrared regions [2, 3]. Another example of a second-order nonlinear process, that is the reverse process of SHG, and the spontaneous counterpart of DFG is called *spontaneous parametric down-conversion* (SPDC) [4, 5]. Unlike DFG, SPDC is mostly used in fundamental research of quantum optics in order to generate coherent photon pairs [6, 7].

An everyday problem in nonlinear optics is that the nonlinear processes in materials are intrinsically weak. Conventionally, this issue is overcome with phase-matching schemes that enable the growth of the nonlinear signal over long enough propagation lengths in the nonlinear medium. This approach is utilized in almost all nonlinear materials varying from quasi-phase-matched crystals to nonlinear optical fibers [3, 8].

In many optical devices, the nonlinear processes are further enhanced by coupling the relevant electromagnetic waves into *optical resonators* [3]. They are optical systems that can store a part of the energy of an electromagnetic wave, when the resonance conditions are fulfilled. The most traditional optical resonators consist of two highly reflective mirrors separated by a specific distance. For this Thesis, we call such systems as *optical cavities*. In addition to their nonlinear applications, optical cavities are widely used in laser systems and spectroscopy due to their highly wavelength-selective operation.[9]

Recent progress in micro- and nanoscale photonics has created a growing demand for the miniaturization of optical components capable of linear and nonlinear processes alike. Novel material type called *metamaterials* have shown the potential for answering this demand. Metamaterials are artificial structures that typically consist of nanoscale structures such as thin films or metal nanoparticles. They exhibit optical properties not found in natural materials such as strong optical activity, epsilon-near-zero behaviour, nanoscale phase-engineering, and magnetism at optical frequencies [10–15]. Studying this type of

novel structures could pave the way towards technologies capable of e.g. optical cloaking, nanoscale lensing, and high-speed optical switching [16, 17].

In addition to their linear properties, the nonlinear properties of metamaterials have been investigated in many studies [18–21]. Especially, plasmonic metasurfaces consisting of metal nanoparticles have recently shown great potential for realizing more efficient nanoscale nonlinear materials. Metal nanoparticles support oscillations of the conduction electrons, known as localized surface plasmons. In resonant conditions, these oscillations increase the local electric field close to the particle. As nonlinear processes scale with higher powers of the local electric field, resonant plasmon oscillations result in a dramatic enhancement of the nonlinear responses of metamaterials.[22, 23]

Despite the recent progress, metamaterials still lack in conversion efficiency when compared against conventional materials. One promising method to improve the efficiency of nonlinear metamaterials is to take advantage of the collective responses of periodic structures known as *surface lattice resonances* (SLRs). They are associated with narrow spectral features known as Rayleigh Anomalies (RA), detected for the first time from a metallic diffraction grating by Wood in 1902 [24]. The narrow linewidths of SLRs imply the presence of the strong the local fields resulting in dramatically enhanced nonlinear processes [25, 26]. The enhancement of nonlinear processes using SLRs has been shown for both plasmonic and dielectric metamaterials [19, 27], and recently, utilizing SLRs in multiresonant conditions has shown potential as a method to reach conversion efficiencies of practical values [28].

However, the multiresonant operation based on SLRs has its drawbacks. For example, the multiresonant conditions are restrictive in terms of polarization of the relevant electric waves. These types of restrictions are undesirable for many nanophotonic applications motivating the search for alternative enhancement methods.

In this Thesis, we propose a novel structure capable of a more flexible multiresonant operation. This design consists of two parts: An optical cavity formed with two distributed Bragg reflectors (DBRs) and a SLR-exhibiting plasmonic metasurface placed inside the cavity. The structure is designed to generate coherent photon pairs via SPDC or to upconversion of the fundamental frequency via SHG. Furthermore, the operation of the structure is flexible in the term of the polarizations of the relevant field. The responses that corrseponding to the allowed polarization combinations are equally strong. Thus, the metamaterial can mimic a conventional nonlinear crystal of type 0, type I, or type II. This property is useful for quantum optics where crystals of type I and especially II are used to generate coherent photon pairs.

Here, we use the finite-domain time-domain (FDTD) method and nonlinear scattering theory (NLST) to estimate both the linear and nonlinear properties of our sample designs. To validate our simulation methods, we first perform proof-of-principle experiments on fully dielectric waveguide gratings (RWGs) and compare the results with simulations conducted on the same structures. We then simulate the properties of a multiresonant

metasurface which we can compare to the results presented in [28], and further validate our simulation methods. Then we repeat the process for the singly-resonant-in-cavity design and compare the results with the multiresonant design.

This Thesis consists of six chapters, this introduction being the first. After this chapter, we introduce the reader to the theoretical background of linear and nonlinear optics. In the third chapter, we will describe the basic properties of optical cavities and metamaterials and how to use them to enhance nonlinear processes. The fourth chapter demonstrates the proof-of-principle studies that we performed on dielectric RWGs. Then, in the fifth chapter, we present novel designs for plasmonic metasurfaces designed for an efficient photon-pair generation with SPDC. In the sixth and final chapter, we conclude by summarizing our results and revealing some future actions.

2 NONLINEAR OPTICS

In this chapter, we examine the basic properties of electromagnetic waves and give an introduction to the basic principles of nonlinear optics. We start by writing down Maxwell's equations of electromagnetism followed by the description of electromagnetic waves. Then, we introduce nonlinear optics via material polarization and focus on second-order nonlinear processes such as second-harmonic generation (SHG) and difference-frequency generation (DFG). From there, we move to describe the classical properties and enhancement methods of the second-order processes. We conclude this chapter with a description of a quantum mechanic nonlinear process called spontaneous parametric down-conversion.

2.1 Maxwell's Equations

In classical physics, light-matter interactions are governed by Maxwell's equations [29]. For macroscopic materials, they can be written as [3, 30]

$$\boldsymbol{\nabla} \cdot \tilde{\mathbf{D}} = \tilde{\rho}_f \,, \tag{2.1}$$

$$\boldsymbol{\nabla} \times \tilde{\mathbf{E}} = -\frac{\partial \tilde{\mathbf{B}}}{\partial t}, \tag{2.2}$$

$$\boldsymbol{\nabla} \cdot \tilde{\mathbf{B}} = 0 \,, \tag{2.3}$$

$$\boldsymbol{\nabla} \times \tilde{\mathbf{H}} = \tilde{\mathbf{J}}_f + \frac{\partial \tilde{\mathbf{D}}}{\partial t} \,, \tag{2.4}$$

where $\tilde{\mathbf{E}}$ is the electric field, $\tilde{\mathbf{B}}$ is the magnetic flux density, $\tilde{\mathbf{D}}$ is the electric displacement, $\tilde{\mathbf{H}}$ is the magnetic field, ρ_f is the free charge density and $\mathbf{J}_f$ is the free current density. The divergence $\boldsymbol{\nabla}\cdot$ and the curl $\boldsymbol{\nabla}\times$ are the vector operators which use the dot and cross products of vectors, respectively. The nabla operator is defined as $\nabla = \hat{\mathbf{i}}\frac{\partial}{\partial x} + \hat{\mathbf{j}}\frac{\partial}{\partial y} + \hat{\mathbf{k}}\frac{\partial}{\partial z}$, where $\hat{\mathbf{i}}$, $\hat{\mathbf{j}}$ and $\hat{\mathbf{k}}$ are the unit vectors along the Cartesian coordinates.

By definition, $\tilde{\mathbf{D}}$ and $\tilde{\mathbf{H}}$ are described by equations [30]

$$\tilde{\mathbf{D}} = \epsilon_0 \tilde{\mathbf{E}} + \tilde{\mathbf{P}} \,, \tag{2.5}$$

$$\tilde{\mathbf{H}} = \frac{\tilde{\mathbf{B}}}{\mu_0} - \tilde{\mathbf{M}} \,, \tag{2.6}$$

where ϵ_0 and μ_0 are the vacuum permittivity and permeability, respectively. Here, the po-

larization field $\tilde{\mathbf{P}}$ and the magnetization field $\tilde{\mathbf{M}}$ are the material responses to the electric and magnetic fields, respectively. From now on, we use tilde ($\sim$) to denote quantities with rapid time variations.

In vacuum, where there are no free currents ($\tilde{\rho}_f = 0$ and $\mathbf{J}_f = 0$) or material responses ($\tilde{\mathbf{P}} = 0$ and $\tilde{\mathbf{M}} = 0$). Then, we can write the electric displacement and the magnetic field as $\tilde{\mathbf{D}} = \epsilon_0 \tilde{\mathbf{E}}$ and $\tilde{\mathbf{H}} = \tilde{\mathbf{B}}/\mu_0$. Now, we can rewrite Equation (2.4) as

$$\boldsymbol{\nabla} \times \tilde{\mathbf{B}} = \epsilon_0 \mu_0 \frac{\partial \tilde{\mathbf{E}}}{\partial t} \,. \tag{2.7}$$

Next, we take the curl of the left-hand side of Equation (2.2). With vector calculus identities and by substituting with Equation (2.1), we then get

$$\boldsymbol{\nabla} \times \boldsymbol{\nabla} \times \tilde{\mathbf{E}} = \nabla(\boldsymbol{\nabla} \cdot \tilde{\mathbf{E}}) - \nabla^2 \tilde{\mathbf{E}} = -\nabla^2 \tilde{\mathbf{E}}. \tag{2.8}$$

By taking the curl of the right-hand side of Equation (2.2) and substituting with Equation (2.7), we get

$$-\boldsymbol{\nabla} \times \frac{\partial \tilde{\mathbf{B}}}{\partial t} = -\frac{\partial}{\partial t} \boldsymbol{\nabla} \times \tilde{\mathbf{B}} = -\epsilon_0 \mu_0 \frac{\partial^2 \tilde{\mathbf{E}}}{\partial t^2}. \tag{2.9}$$

As Equations (2.8) and (2.9) are the curls of the left- and right-hand sides of the same equation, we can combine them and get the electromagnetic wave equation

$$\nabla^2 \tilde{\mathbf{E}} = \epsilon_0 \mu_0 \frac{\partial^2 \tilde{\mathbf{E}}}{\partial t^2} \,. \tag{2.10}$$

The equation above is of a similar structure than the general wave equation

$$\nabla^2 \Psi = \frac{1}{v^2} \frac{\partial^2 \Psi}{\partial t^2}, \tag{2.11}$$

where Ψ is the wave function and v is the propagation speed of the wave. By comparing Equations (2.10) and (2.11) we can define the vacuum speed of light as [31]

$$c_0 = \frac{1}{\sqrt{\epsilon_0 \mu_0}}. \tag{2.12}$$

2.2 Electromagnetic Waves

In addition to the classical wave nature, light is also described as massless particles called photons. A photon is associated with a quantified energy $E_p = h\nu$ and momentum $p = \frac{h}{\lambda}$, where h is the Planck's constant, and ν and λ are the frequency and wavelength of the corresponding electromagnetic wave, respectively. Now, it is convenient to define light as a monochromatic plane wave propagating along the z-axis. Then, the electric field can be written as

$$E(z,t) = E_0 e^{i(kz - \omega t)} + c.c. \,, \tag{2.13}$$

where E_0 is the field amplitude, $k = \frac{2\pi}{\lambda}$ is the propagation number, z is the position along the z-axis, $\omega = 2\pi\nu$ is the angular frequency, t is time and $c.c.$ denotes the complex conjugate of the first term. The speed of such a wave is given by equation

$$c = \frac{\omega}{k} = \frac{\omega}{nk_0} = \frac{c_0}{n}, \tag{2.14}$$

where n is the refractive index of the medium and k_0 is the propagation number in vacuum.

We now move to describe the electric field in three dimensions by introducing the propagation vector

$$\mathbf{k} = k_x\hat{\mathbf{i}} + k_y\hat{\mathbf{j}} + k_z\hat{\mathbf{k}}\,. \tag{2.15}$$

The propagation number is equal to the absolute value of $\mathbf{k}$ and is hence connected to the Cartesian components through equation

$$k = |\mathbf{k}| = \sqrt{k_x^2 + k_y^2 + k_z^2}. \tag{2.16}$$

Now, the electric field becomes a vector quantity written as a function of the position vector $\mathbf{r}$:

$$\tilde{\mathbf{E}}(\mathbf{r}, t) = \mathbf{E}_0 e^{i(\mathbf{k}\cdot\mathbf{r}-\omega t)} + c.c. = E_0\hat{\mathbf{p}}e^{i(\mathbf{k}\cdot\mathbf{r}-\omega t)} + c.c. \tag{2.17}$$

Here, the field amplitude $\mathbf{E}_0 = E_0\hat{\mathbf{p}}$ is also a vector quantity whose direction is defined by the unit vector $\hat{\mathbf{p}}$, also known as the polarization vector (not to be confused with the material response to the electric field). Hence, $\hat{\mathbf{p}}$ defines the direction in which $\tilde{\mathbf{E}}$ oscillates with respect to space and time.

Next, we define the oscillation direction of the electric field with respect to the axis of propagation. We assume an isotropic material where the electric field is divergenceless ($\boldsymbol{\nabla}\cdot\tilde{\mathbf{E}}(\mathbf{r}, t) = 0$). We apply this assumption to the electric field defined in Equation (2.17) and get the equation

$$\boldsymbol{\nabla}\cdot\tilde{\mathbf{E}}(\mathbf{r}, t) = iE_0\mathbf{k}\cdot\hat{\mathbf{p}}e^{i(\mathbf{k}\cdot\mathbf{r}-\omega t)} + c.c. = i\mathbf{k}\cdot\tilde{\mathbf{E}}(\mathbf{r}, t) = 0. \tag{2.18}$$

This illustrates that the electric field is perpendicular to the propagation direction, which means that the plane wave $\tilde{\mathbf{E}}(\mathbf{r}, t)$ is transverse in isotropic media.

Next, we construct a connection between the electric and magnetic field components of the electromagnetic wave. We start by substituting the electric field from Equation (2.17) into Equation (2.2) and rewriting it as

$$\boldsymbol{\nabla}\times\tilde{\mathbf{E}}(\mathbf{r}, t) = i\mathbf{k}\times\tilde{\mathbf{E}}(\mathbf{r}, t) = -\frac{\partial\tilde{\mathbf{B}}(\mathbf{r}, t)}{\partial t}. \tag{2.19}$$

Now, integrating both sides over time results in

$$\tilde{\mathbf{B}}(\mathbf{r}, t) = \frac{\mathbf{k}}{\omega}\times\tilde{\mathbf{E}}(\mathbf{r}, t). \tag{2.20}$$

From Equations (2.18) and (2.20) follows that electric and magnetic fields are mutually

perpendicular, making planar electromagnetic waves transverse. Additionally, their amplitudes are connected by equation

$$\left|\tilde{\mathbf{B}}(\mathbf{r},t)\right| = B_0 = \frac{n}{c_0}E_0, \tag{2.21}$$

where n is the refractive index of the medium.[31, 32]

2.3 Irradiance

Our ability to detect electromagnetic waves is based on their capability to transfer energy and momentum. Therefore, the conventional measured quantity of light is its energy flow per unit time per unit area, also know as *irradiance* [31], sometimes called intensity. The power transferred with the electromagnetic wave is described with the Poynting vector [31]

$$\tilde{\mathbf{S}} = c^2\epsilon_0\tilde{\mathbf{E}} \times \tilde{\mathbf{B}}. \tag{2.22}$$

Its magnitude $\tilde{S}$ is the power per unit area through a surface perpendicular to $\tilde{\mathbf{S}}$, and it can be written as

$$\tilde{S} = c^2\epsilon_0\left|\tilde{\mathbf{E}} \times \tilde{\mathbf{B}}\right|, \tag{2.23}$$

whose time average is the irradiance of light. Next, we use Equations (2.21) and (2.23) to calculate the irradiance with equation

$$I = \langle S\rangle_T = \frac{nc_0\epsilon_0}{2}E_0^2\,, \tag{2.24}$$

which we use later to describe properties of laser systems and nonlinear interactions.[31] Furthermore, Equation (2.24) connects irradiance to the amplitude of the electric field. Thus, we can neglect the magnetic interactions and focus on the material responses to the electric field component of light. In most cases, this selection is justified, as the magnetic interactions typically have negligible impact on the light-matter interactions.

2.4 Nonlinear Polarization in Materials

When light enters a medium, its electric field induces electric dipoles into the material. The total sum of the induced dipole moments is the *polarization* field $\tilde{\mathbf{P}}(\mathbf{r},t)$ [8]. Typically, $\tilde{\mathbf{P}}(\mathbf{r},t)$ is linearly dependent on the incident electric field and is thus given by the following integral [33]:

$$\tilde{\mathbf{P}}(\mathbf{r},t) = \epsilon_0\int_{-\infty}^{\infty}\int_{-\infty}^{\infty}\tilde{\chi}^{(1)}(\mathbf{r}-\mathbf{r}',t-t')\cdot\tilde{\mathbf{E}}(\mathbf{r}',t')\mathrm{d}\mathbf{r}'\mathrm{d}t', \tag{2.25}$$

where $\tilde{\chi}^{(1)}(\mathbf{r}-\mathbf{r}', t-t')$ is the linear susceptibility which is a tensor of rank two. The convolution above can be simplified by defining the Fourier transforms over space

$$\mathcal{F}\{f(\mathbf{r})\} = \int_{-\infty}^{\infty} f(\mathbf{r}) e^{i\mathbf{k}\cdot\mathbf{r}} \mathrm{d}\mathbf{r} \tag{2.26}$$

and time

$$\mathcal{F}\{f(\mathbf{t})\} = \int_{-\infty}^{\infty} f(\mathbf{r}) e^{-i\omega t} \mathrm{d}t. \tag{2.27}$$

By recalling the convolution theorem, Equation (2.25) is now written as

$$\mathbf{P}(\mathbf{k},\omega) = \epsilon_0 \chi^{(1)}(\mathbf{k},\omega) \cdot \mathbf{E}(\mathbf{k},\omega), \tag{2.28}$$

where

$$\chi^{(1)}(\mathbf{k},\omega) = \mathcal{F}\{\tilde{\chi}^{(1)}(\mathbf{r},t)\} \tag{2.29}$$

and

$$\mathbf{E}(\mathbf{k},\omega) = \mathcal{F}\{\tilde{\mathbf{E}}(\mathbf{r},t)\}. \tag{2.30}$$

The susceptibilities and electric fields are usually independent of spatial quantities $\mathbf{r}$ and $\mathbf{k}$ [33]. Hence, we focus on t and ω domains and rewrite Equation (2.28) as

$$\mathbf{P}(\omega) = \epsilon_0 \chi^{(1)}(\omega) \cdot \mathbf{E}(\omega), \tag{2.31}$$

which indicates that polarization oscillates at the same frequency as the incident field. Furthermore, the form in Equation (2.31) allows us to describe the material dispersion conveniently by recalling that

$$n^2 = 1 + \chi^{(1)}. \tag{2.32}$$

For weak enough incident fields, Equations (2.25) and (2.31) describe the material response with adequate accuracy. However, with strong enough incident fields, $\tilde{\mathbf{P}}(t)$ should be written as a power series of $\tilde{\mathbf{E}}(t)$ by equation [33]

$$\begin{aligned}\tilde{\mathbf{P}}(t) =& \epsilon_0 \left(\int_{-\infty}^{\infty} \tilde{\chi}^{(1)}(t-t') \cdot \tilde{\mathbf{E}}(t') \mathrm{d}t' \right. \\ &+ \int_{-\infty}^{\infty} \tilde{\chi}^{(2)}(t-t_1; t-t_2) \cdot \tilde{\mathbf{E}}(t_1) \cdot \tilde{\mathbf{E}}(t_2) \mathrm{d}t_1 \mathrm{d}t_2 \\ &\left. + \int_{-\infty}^{\infty} \tilde{\chi}^{(3)}(t-t_1; t-t_2; t-t_3) \cdot \tilde{\mathbf{E}}(t_1) \cdot \tilde{\mathbf{E}}(t_2) \cdot \tilde{\mathbf{E}}(t_3) \mathrm{d}t_1 \mathrm{d}t_2 \mathrm{d}t_3 + \cdots, \right.\end{aligned} \tag{2.33}$$

where $\chi^{(n)}$ is the nth-order susceptibility tensor with rank $n+1$. Usually, $\tilde{\mathbf{E}}(t)$ can be expressed as a group of monochromatic plane waves

$$\tilde{\mathbf{E}}(t) = \sum_i \mathbf{E}(\omega_i), \tag{2.34}$$

which is essentially the Fourier transform of $\tilde{\mathbf{E}}(t)$. Similarly, the Fourier transform of

Equation (2.33) gives

$$\mathbf{P}(\omega) = \mathbf{P}^{(1)}(\omega) + \mathbf{P}^{(2)}(\omega) + \mathbf{P}^{(3)}(\omega) + \cdots , \tag{2.35}$$

with nonlinear polarization [33]

$$\mathbf{P}^{(n)}(\omega) = \epsilon_o \chi^{(n)} \left(\omega = \sum_i \omega_i \right) \prod_i \mathbf{E}(\omega_i). \tag{2.36}$$

The nonlinear processes related to $\tilde{\mathbf{P}}^{(n\geq 2)}$ are intrinsically weak. Thus, the traditional nonlinear applications utilize the second- and third-order nonlinear effects [3, 9]. In this Thesis, we focus on the second-order effects and leave other effects for future studies to cover.

2.5 Second-order Nonlinear Processes

In second-order processes, new frequencies are created in a nonlinear medium via three-wave mixing interactions. In order to explain the different wave mixing processes, we consider a situation where an electric field consisting of two monochromatic field components is incident upon a second-order nonlinear material. The two components have distinct frequencies ω_1 and ω_2, and thus the incident electric field is given by

$$\tilde{\mathbf{E}}(t) = \mathbf{E}_1 e^{-i\omega_1 t} + \mathbf{E}_2 e^{-i\omega_2 t} + c.c. = \mathbf{E}(\omega_1) + \mathbf{E}(\omega_2) + c.c. \tag{2.37}$$

Now, the second-order polarization is given by

$$\tilde{\mathbf{P}}^{(2)}(t) = \epsilon_0 \chi^{(2)} \tilde{\mathbf{E}}^2(t), \tag{2.38}$$

and also by

$$\tilde{\mathbf{P}}^{(2)}(t) = \sum_n \mathbf{P}(\omega_n) e^{-i\omega_n t}. \tag{2.39}$$

In the frequency domain, the various second-order polarization components can be written as [3]

$$\mathbf{P}^{(2)}(2\omega_1) = \epsilon_0 \chi^{(2)}(2\omega_1; \omega_1, \omega_1)\mathbf{E}_1^2 , \tag{2.40}$$

$$\mathbf{P}^{(2)}(2\omega_2) = \epsilon_0 \chi^{(2)}(2\omega_2; \omega_2, \omega_2)\mathbf{E}_2^2 , \tag{2.41}$$

$$\mathbf{P}^{(2)}(\omega_1 + \omega_2) = 2\epsilon_0 \chi^{(2)}(\omega_1 + \omega_2; \omega_1, \omega_2)\mathbf{E}_1\mathbf{E}_2 , \tag{2.42}$$

$$\mathbf{P}^{(2)}(\omega_1 - \omega_2) = 2\epsilon_0 \chi^{(2)}(\omega_1 - \omega_2; \omega_1, -\omega_2)\mathbf{E}_1\mathbf{E}_2^* , \tag{2.43}$$

$$\mathbf{P}^{(2)}(0) = 2\epsilon_0 \left(\chi^{(2)}(0; \omega_1, -\omega_1)\mathbf{E}_1\mathbf{E}_1^* + \chi^{(2)}(0; \omega_2, -\omega_2)\mathbf{E}_2\mathbf{E}_2^* \right) . \tag{2.44}$$

Here, the complex conjugates are connected to the frequency components with negative frequencies by $E^*(\omega) = E(-\omega)$. Thus, we can omit the negative frequency counterparts of Equations (2.40)–(2.43), since they are the complex conjugates of the mentioned equa-

tions.

$\mathbf{P}^{(2)}(0)$ corresponds to optical rectification, a process where a static electric field is created into the medium but is not a subject of interest here. The other four polarization components in Equations (2.40)–(2.43) correspond to the physical processes where new frequency components are created and thus are much more relevant for this Thesis. $\mathbf{P}^{(2)}(2\omega_1)$ and $\mathbf{P}^{(2)}(2\omega_2)$ correspond to SHG, $\mathbf{P}^{(2)}(\omega_1 + \omega_2)$ to sum-frequency generation (SFG), and $\mathbf{P}^{(2)}(\omega_1 - \omega_2)$ to DFG. Next, we will describe the photon interactions of these processes and visualize them with energy diagrams shown in Figures 2.1–2.3. In the energy diagrams, the solid and dashed lines represent atomic ground states and virtual levels, respectively. The upward and upward arrows illustrate the excitation and relaxation of the system, respectively.

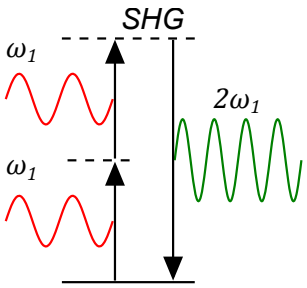

Figure 2.1. *The energy diagram of second-harmonic generation (SHG). Two incident photons with frequency ω_1 excite the system to a virtual state. The system immediately relaxes from the virtual state, and a photon with doubled frequency $2\omega_1$ is generated.*

In SHG, the two fundamental photons with frequency ω_1 are absorbed in to the nonlinear medium. The system is then excited to a virtual state with the combined energy of the two incident photons. When the system relaxes from the virtual state, a photon with the doubled frequency of $2\omega_1$ is generated. As the relaxation from the virtual state is instant, the generated photon is coherent with the fundamental photons.

In the proper circumstances, SHG leads to a full frequency conversion from ω_1 to $2\omega_1$. Thus, SHG is widely used to convert laser power to a different spectral region. The most common example is a typical laser pointer where an infrared emission from the laser is converted to the visible region via SHG.[3]

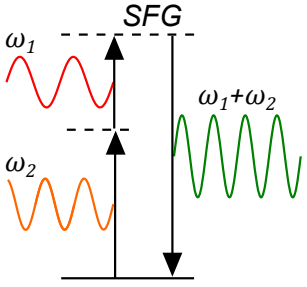

Figure 2.2. *The energy diagram of sum-frequency generation (SFG). Two photons with frequencies ω_1 and ω_2 interact with the system resulting into a emission of a photon with frequency $\omega_1 + \omega_2$.*

The mechanism of SFG is very similar to SHG, as is shown in Figure 2.2. The only difference is that the two incident photons have distinct frequencies of ω_1 and ω_2. Thus, the generated photon has the frequency $\omega_1 + \omega_2$. Unlike SHG that is typically used for frequency conversion of fixed-frequency lasers, SFG is used to realize tunable light sources. For example, illuminating a nonlinear medium with two visible-region lasers leads to the generation of ultraviolet light via SFG. When one of the incident lasers is frequency-tunable, the result is a frequency-tunable laser operating in the ultraviolet region.

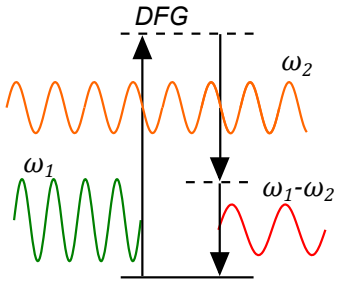

Figure 2.3. *The energy diagram of difference-frequency generation (DFG). An incident photon with frequency ω_1 excite the system to a virtual state. The other incident photon with frequency ω_2 initiates stimulated emission resulting in gain at the input frequency ω_2. The remaining energy is emitted as a third photon with frequency $\omega_1 - \omega_2$.*

DFG differs from the other two processes as of the two incident photons only one is absorbed in the process. The other of the incident photons causes stimulated emission and thus gain at the frequency ω_2. In addition, a new photon is generated at the frequency $\omega_1 - \omega_2$. Similar SFG, DFG is also used to create tunable laser sources. Via DFG, illuminating a nonlinear medium with two visible-region lasers leads to the generation of infrared light. If one of the input laser is again frequency-tunable, the result of DFG is a frequency-tunable laser operating in the infrared region. This methods is used e.g. in optical parametric oscillators which we describe in more detail in Section 3.2.

For all the processes described above, the emitted electric field at the generated frequency is proportional to to the second-order polarization $\tilde{\mathbf{P}}^{(2)}$. Thus e.g. for SHG, the emitted irradiance I_{SHG} can be written to be proportional the irradiance I_0 of the fundamental field and the second-order susceptibility tensor $\chi^{(2)}(2\omega_1;\omega_1,\omega_1)$ resulting in equation [32]

$$I_{SHG} \propto I_0^2 \left| \chi^{(2)}(2\omega_1;\omega_1,\omega_1) \right|^2. \tag{2.45}$$

The square-dependence on I_0 is one of the basic characteristics of SHG, which is widely used to identify a generated signal as SHG [19, 34].

2.6 Second-order Susceptibility

The Lorentz model describes atoms as systems where light electrons are connected to much heavier nuclei with a spring. When an electromagnetic field interacts with the atom,

it induces displacement $\tilde{x}(t)$ to the electrons creating an atomic dipole moment $p(t) = -e\tilde{x}(t)$. When the incident field is assumed to be monochromatic, the displacement can be written as [3]

$$\tilde{x}(t) = x^{(1)}(\omega)e^{-i\omega t}. \tag{2.46}$$

The amplitude $x^{(1)}(\omega)$ is defined as

$$x^{(1)}(\omega) = -\frac{e}{m}\frac{E(\omega)}{D(\omega)}, \tag{2.47}$$

where e is the charge and m is the mass of the electron. The denominator function $D(\omega)$ is defined as

$$D(\omega) = \omega_0^2 - \omega^2 - 2i\omega\gamma, \tag{2.48}$$

where ω_0 is the resonance frequency of the material and γ is the damping constant that is related to the linewidth of the material resonance.

The amplitude of linear polarization is given as the total sum of atomic dipole moments. This sum can be calculated by defining the average number density of atoms as N, allowing to write the polarization as

$$P^{(1)} = -Nex^{(1)}(\omega)\,. \tag{2.49}$$

With Equations (2.31), (2.47), and (2.49) we discover that the linear susceptibility is given by

$$\chi^{(1)}(\omega) = \frac{N(e^2/m)}{\epsilon_0 D(\omega)}. \tag{2.50}$$

Similar analogy can be used for $P^{(2)}$, and thus, the second-order susceptibility corresponding to the process of SHG can be written as [3]

$$\chi^{(2)}(2\omega;\omega,\omega) = \frac{N(e^3/m^2a)}{D(2\omega)D^2(\omega)}, \tag{2.51}$$

where a is a nonlinear parameter for the Lorentz's model and of the order of the size of the atom ($a \sim 10^{-10}$) [3].

By comparing Equations (2.50) and (2.51), we find that $\chi^{(2)}(2\omega;\omega,\omega)$ is also given by

$$\chi^{(2)}(2\omega;\omega,\omega) = \frac{\epsilon_0^2 ma}{N^2e^3}\chi^{(1)}(2\omega)\left[\chi^{(1)}(\omega)\right]^2. \tag{2.52}$$

The quantity $\frac{\epsilon_0^2 ma}{N^2e^3}$ is nearly a constant for all condensed matter [3]. Now, we mark this constant as Δ and solve it from Equation (2.52) as [3, 33]

$$\Delta = \frac{\chi^{(2)}(2\omega;\omega,\omega)}{\chi^{(1)}(2\omega)\left[\chi^{(1)}(\omega)\right]^2}. \tag{2.53}$$

The constant Δ is commonly known as *Miller's delta*, and the equality in Equation (2.53) as the *Miller's rule*. With Equations (2.48), (2.50), and (2.53) we can now draw two

conclusions. The first conclusion is that at non-resonant conditions ($\omega_0 >> \omega$), where the material is rather lossless, the second-order processes are quite weak as $\chi^{(2)} \simeq 6.9 \times 10^{-12}$ m/V [3]. As the second consequence, we notice that in resonant conditions ($\omega_0 \approx \omega$) highly refractive materials have high values for $\chi^{(2)}$. This latter consequence we exploit later when we describe some enhancement methods for SHG in nanoscale structures.

2.7 Birefringence and Second-harmonic Generation

As we mentioned before, $\chi^{(1)}$ is a second rank tensor whose components are defined by the oscillation directions of $\mathbf{P}^{(1)}(\omega)$ and $\mathbf{E}(\omega)$. Thus, it is convenient to rewrite Equation (2.31) for the amplitudes of different field components as

$$P_i^{(1)}(\omega) = \epsilon_0 \sum_j \chi_{ij}^{(1)} E_j(\omega), \tag{2.54}$$

where indices i and j mark the field components. In the linear regime, the formed dipoles are for most materials aligned with the fundamental field. Therefore, Equation (2.54) simplifies to

$$P_i^{(1)}(\omega) = \epsilon_0 \chi_{ii}^{(1)} E_i(\omega). \tag{2.55}$$

Next, we apply a similar analogy to $\chi^{(2)}$ which is a third rank tensor. Then, it is convenient to write an equation for a second-harmonic field component as

$$P_i^{(2)}(2\omega) = \epsilon_0 \sum_{jk} \chi_{ijk}^{(2)} E_j(\omega) E_k(\omega). \tag{2.56}$$

Now, we can rewrite the Miller's rule as [33]

$$\Delta_{ijk} = \frac{\chi_{ijk}^{(2)}(2\omega;\omega,\omega)}{\chi_{ii}^{(1)}(2\omega)\chi_{jj}^{(1)}(\omega)\chi_{kk}^{(1)}(\omega)}, \tag{2.57}$$

where the notation $\chi(2\omega;\omega,\omega)$ clarifies the fact that the nonlinear material response depends both of the input frequency ω and of the signal frequency ω. Here, we notice that Equations (2.32) and (2.57) connect $\chi_{ijk}^{(2)}(2\omega;\omega,\omega)$ to the material *birefringence*, i.e. to the polarization dependence of the refractive index.

2.8 Symmetry Requirements of Second-order Effects

As a third rank tensor, $\chi^{(2)}$ consists of 27 different Cartesian components. For some crystal point-groups, defined by group theory, all the components can be non-zero and independent of each other. In most materials, the number of allowed tensor components is significantly reduced by permutation and symmetry properties of $\chi^{(2)}$. For simplicity,

we demonstrate this for the SHG tensor $\chi^{(2)}_{ijk}(2\omega;\omega,\omega)$ but note that similar restrictions apply also for other second-order processes.[3]

First, we note that the fundamental field factors in Equation (2.56) are both identical and interchangeable. Thus, the permutation of the last two indices will not change the process in any way and we can write that [3]

$$\chi^{(2)}_{ijk}(2\omega;\omega,\omega) = \chi^{(2)}_{ikj}(2\omega;\omega,\omega). \tag{2.58}$$

As mentioned before, the conventional nonlinear materials are lossless at the operating frequencies ω and 2ω. As a consequence, we can permute all of the indices of the SHG tensor as long as we permute the corresponding frequencies as well. In other words, we can write that

$$\chi^{(2)}_{ijk}(2\omega;\omega,\omega) = \chi^{(2)}_{jik}(\omega;2\omega,-\omega), \tag{2.59}$$

which holds as long as the first frequency argument is the sum of the latter two. This equality is called the full permutation symmetry which can be used even further, if ω and 2ω are significantly smaller than the lowest resonant frequency of the material. Then, we can neglect the frequency dependencies and permute all of the indices of the SHG tensor freely:

$$\chi^{(2)}_{ijk} = \chi^{(2)}_{jik} = \chi^{(2)}_{kji} = \chi^{(2)}_{ikj} = \chi^{(2)}_{jki} = \chi^{(2)}_{kij}, \tag{2.60}$$

which is also known as Kleinman symmetry [35]. Even though the frequency-independent behaviour is not fulfilled in the results presented in this work, Kleinman symmetry is still a valid example to illustrate the properties of the SHG tensor.

Last, the SHG tensor components are restricted by the symmetry properties of the nonlinear medium. If the medium has inversion symmetry with respect to $\mathbf{r}$, then the transformation $\mathbf{r} \longrightarrow \mathbf{r}'$ should not impact $\chi^{(2)}$. We now consider the situation where the sign of $\mathbf{r}$ is reversed. Now, the electric field $\mathbf{E}$ and the polarization field $\mathbf{P}$ are polar vectors that are odd under the inversion transformation. Therefore, also change their signs in the inversion operation. In other words, we apply the following transformations:

$$\mathbf{r} \longrightarrow -\mathbf{r}, \tag{2.61}$$

$$\mathbf{E} \longrightarrow -\mathbf{E}, \tag{2.62}$$

$$\mathbf{P} \longrightarrow -\mathbf{P}. \tag{2.63}$$

Next, we assume that the nonlinear polarization is written as

$$\mathbf{P} = \epsilon_0 \chi^{(2)} \mathbf{E}^2. \tag{2.64}$$

Now, by applying the inversion operator and the transformation properties of E and P on the above situation, we can write the following equality:

$$-\mathbf{P} = \epsilon_0 \chi^{(2)} (-\mathbf{E})^2 = \epsilon_0 \chi^{(2)} \mathbf{E}^2 = \mathbf{P}, \tag{2.65}$$

which can only hold true if $\mathbf{P}$ vanishes identically. From here we can conclude that [3]

$$\chi^{(2)} = 0. \tag{2.66}$$

Equation (2.66) has a powerful consequence: For any second-order processes to occur, the inversion symmetry must be broken which forbids all second-order processes in centrosymmetric media. However, the inversion symmetry is broken at interfaces and in some crystal structures, in which case the symmetry requirements drastically limit the number of non-zero components. Conventionally, the number of non-zero and independent tensor components is less than ten for SHG. [3]

2.9 Local-field Enhancement and Phase-matching Effects

The conventional nonlinear crystals used in second-order processes are practically lossless at the operating frequencies. According to the Miller's rule, they have then low values for $\chi^{(2)}$ and thus weak second-order responses. Fortunately, it is possible to enhance nonlinear processes with local electric fields. This effect is called *local-field enhancement* which is usually phenomenologically described by using the local-field $E_{loc}(\omega)$. Now, we can replace the linear susceptibilities in Equation (2.52) by $E_{loc}(2\omega)\chi^{(1)}(2\omega)$ and $E_{loc}(\omega)\chi^{(1)}(\omega)$ [33]. Then, the SHG irradiance I_{SHG} should scale as [36]

$$I_{SHG} \propto |E_{loc}(2\omega)|^2 \left|E_{loc}^2(\omega)\right|^2. \tag{2.67}$$

In conventional nonlinear materials, the local electric field is enhanced with the fields generated in the previous parts of the nonlinear medium. This, however, requires constructive interaction between the relevant electric fields. This, on the other hand, requires vanishing or compensation of *wavevector mismatch* Δk. For SHG, Δk is defined with equation

$$\Delta k = 2k_1 - k_2, \tag{2.68}$$

with [3]

$$k_i = \frac{n(\omega_i)\omega_i}{c}. \tag{2.69}$$

The perfect phase-matching ($\Delta k = 0$) requires that $n(\omega_1) = n(2\omega_1)$, which is impossible for traditional dispersive materials where the refractive index increases monotonically with frequency. Conventionally, this is overcome with the use of *birefringent* or *quasi-phase-matched* crystals. For phase-matched materials, the SH irradiance becomes square-dependent on the propagation length in the material. [3] If the phase-matching condition is not fulfilled, the SH irradiance oscillates as a function of propagation length in the nonlinear medium [3, 37].

For second-order processes, there are three different types of phase-matched materials, named as *type 0*, *type I* and *type II*. As is shown in Figure 2.4, these three types differ

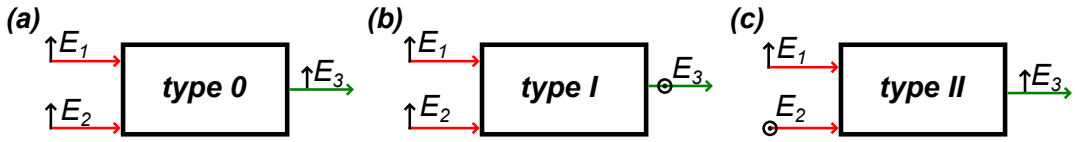

Figure 2.4. *Three different types of phase-matched crystals used to convert input fields E_1 and E_2 to an output field E_3 via second-order nonlinear processes.* ***(a)*** *In type 0, all the relevant field have the same polarization.* ***(b)*** *In type I material or crystal, E_1 and E_2 have the same polarization which is orthogonal to the polarization of E_3.* ***(c)*** *In type II, E_3 has the same polarization than one of the input fields which have orthogonal polarizations.*

in the polarizations of the interacting fields. Type 0 crystals are phase-matched for processes where the incident and generated fields have the same polarization. For type I, the incident field is orthogonal to the generated, and for type II the two generated fields have orthogonal polarizations. Especially, crystals of types I and II are widely used in nonlinear applications such as in optical parametric oscillators and photon-pair sources for quantum optics.[3]

2.10 Spontaneous Parametric Down-conversion

So far, we have introduced SHG, SFG and DFG which all are classical *stimulated* processes. The stimulation occurs with the frequencies that were generated in earlier in the nonlinear medium and the signal is enhanced as described in Section 2.9. These processes have their corresponding *spontaneous* quantum processes where only the fundamental photons are present [5]. For DFG, the corresponding quantum process is called *spontaneous parametric down-conversion* (SPDC), also known as parametric fluorescence [3].

The mechanism of SDPC, as is shown in Figure 2.5, is similar to DFG with a difference that only the pumping frequency $\omega_3 = \omega_1 + \omega_2$ is present in the beginning of the process. This makes SPDC a *reverse* process of SFG, and thus it follows the phase-matching condition of SFG ($k_1 + k_2 = k_3$) rather than that of DFG ($k_1 - k_2 = k_3$) [38–40]. Furthermore, it is more convenient to describe SPDC with the susceptibility of SFG ($\chi^{(2)}(\omega_1 + \omega_2; \omega_1, \omega_2)$) than with the DFG-tensor ($\chi^{(2)}(\omega_1 - \omega_2; \omega_1, -\omega_2)$). Consequently, by investigating the processes of SHG, DFG and SFG occurring in a material, one can also deduce information of the SPDC response of the material [5].

Like any spontaneous processes, SPDC is relatively weak in comparison with stimulated processes. In phase-matched crystals, the stimulated processes are square-dependent on the propagation length L while SPDC irradiance typically scales as $I_{SPDC} \propto L^{\frac{3}{2}}$ [5]. Thus, SPDC is not usually used in nonlinear applications such as in optical parametric oscillators. However, *degenerate* SPDC where the generated photons have the same frequency, i.e. the reverse process of SHG, is a reliable process to generate coherent photon pairs. Therefore, degenerate SPDC is widely used in quantum optics as a photon-pair source [6, 7, 41]. There, two types of phase-matched crystals are used: Type I to

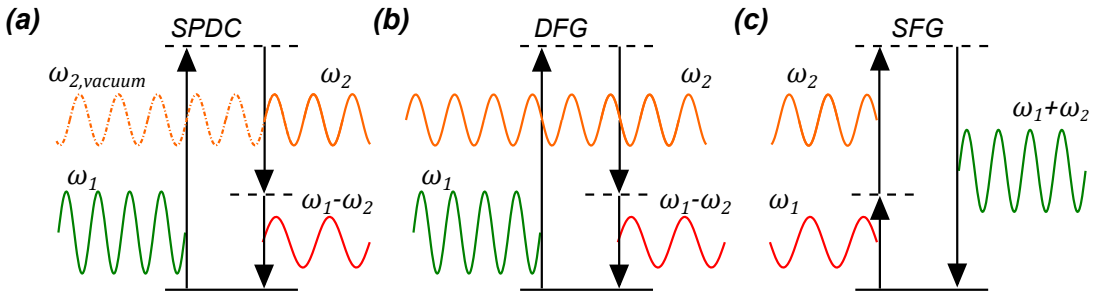

Figure 2.5. *Energy diagrams of* ***(a)*** *spontaneous parametric down-conversion (SPDC),* ***(b)*** *difference-frequency generation (DFG), and* ***(c)*** *sum-frequency generation (SFG). DFG and SFG are the stimulated and reversed processes of SPDC, respectively.*

generate photon pairs with polarization orthogonal to the pump, and type II to generate photon pairs where the two signal photons have orthogonal polarization to each other.

In the applications of quantum optics however, the common difficulties arise from the bandwidth of the nonlinear crystal and the resulting inaccuracies of the photon-pair coherence. Later in this Thesis, we will propose a novel nanoscale structure as a solution to this issue. In our structure, SPDC will be enhanced using methods that are shown to be effective for SHG [19, 27] and are described in detail in the next chapter.

3 OPTICAL RESONATORS IN NONLINEAR OPTICS

In this chapter, we give a short introduction to optical resonators and their applications that use nonlinear optics. Optical resonators are systems that can store the energy of the incident electromagnetic field. From now on, we shall focus on two types of resonators: optical cavities formed with two or more mirrors, and resonant metamaterials with high-quality material responses. We start our treatment with an example of a macroscale cavity and its properties, followed by a design of a similar microcavity formed with distributed Bragg reflectors (DBRs). Then, we give an illustrative example of an optical parametric oscillator (OPO) that uses an optical cavity to enhance DFG of a nonlinear material. From there, we move to metasurfaces and introduce their most relevant material responses: localized surface plasmon resonances and surface lattice resonances. For these resonances, we then define the same properties that were introduced with macroscale cavities. As a conclusion to this chapter, we demonstrate how these lattice resonances have been used to enhance SHG from metasurfaces.

3.1 Optical Cavities

We start our description of optical resonators with a widely used and relatively simple cavity design called *Fabry–Pérot etalon* (FP), illustrated in Figure 3.1. This type of cavity is formed with two highly reflective plane mirrors, with reflectances R_1 and R_2. The mirrors are separated by a distance L in a medium with a refractive index of n. Traditionally, FP etalons are used as laser cavities and as wavelength-selective elements in spectroscopy and nonlinear optical devices, but more recently, cavities with spherical mirrors are preferred due to their superior stability. Nevertheless, a FP etalon is a simple and illustrative example to define many useful properties for optical resonators.[3, 9]

For efficient coupling, the fundamental light in the cavity must be self-consistent. This turns into a requirement that the round-trip phase shift

$$\Delta\phi = -2kL + \phi, \tag{3.1}$$

where $-2kL$ arise from the propagation and ϕ from the internal phase shifts, must be an integer multiplier of 2π. We assume a lossless medium and that the reflections from the cavity mirrors induce a total phase shift of 2π. We can now derive a connection between

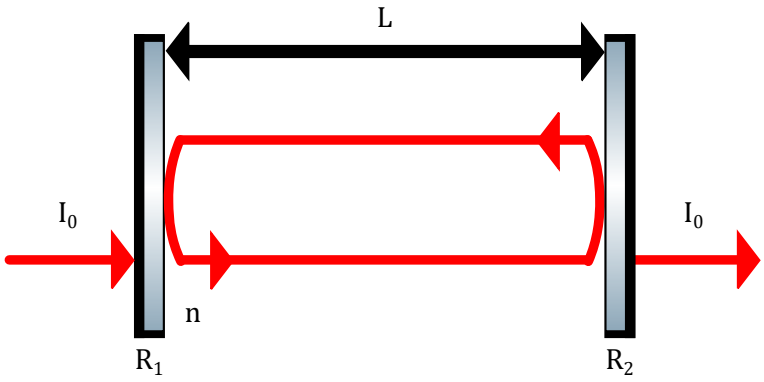

Figure 3.1. *A FP etalon formed with two planar mirrors with reflectances R_1 and R_2. The mirrors are separated by the distance L in a medium with refractive index n. The etalon is designed to transmit irradiance I_0 when the coupling conditions are fulfilled.*

the effective length $L' = nL$ of the cavity and the fundamental wavelength λ as

$$L' = m\frac{\lambda}{2}, \tag{3.2}$$

where m is an integer.[9]

The spectral properties of optical cavities are commonly described in terms of frequencies rather than in wavelengths. As a start, we define the mode frequency ν_m that can be trivially derived from Equation (3.2) as follows

$$\nu_m = m\frac{c}{2L'}. \tag{3.3}$$

The adjacent cavity modes are then separated by *the free spectral range* [9]

$$\Delta\nu_{fsr} = \frac{c}{2L'}. \tag{3.4}$$

Note, that $\Delta\nu_{fsr}$ is also the smallest possible value for ν_m and thus corresponds to the longest possible coupled wavelength.

Even though these cavity modes are self-consistent, they experience losses during every round-trip due to the transmission through the cavity mirrors. This leads to exponential decay in the field intensity described by equation

$$I(t) \simeq e^{-t/\tau_c} I(0). \tag{3.5}$$

The cavity photon lifetime τ_c can be described in terms of cavity parameters as given by

$$\tau_c = -\frac{2L'}{c\ln(R_1R_2)}. \tag{3.6}$$

Note, that τ_c has always positive values since $\ln(R_1R_2) \leq 0$. [9]

Now, the Fourier transform of Equation (3.6) gives the linewidth $\Delta\nu_c$ of the cavity modes

as

$$\Delta\nu_c = \frac{1}{2\pi\tau_c}. \tag{3.7}$$

By combining Equations (3.4), (3.6) and (3.7) we can also write that

$$\Delta\nu_c = -\frac{\Delta\nu_{fsr}\ln(R_1R_2)}{2}. \tag{3.8}$$

With typical reflectance values ($0.9 \leq R_{1,2} \leq 1$) this indicates that $\Delta\nu_{fsr} \gg \Delta\nu_c$ which is required to avoid mode overlapping.[9] The spectral properties of a FP etalon are illustrated in Figure 3.2.

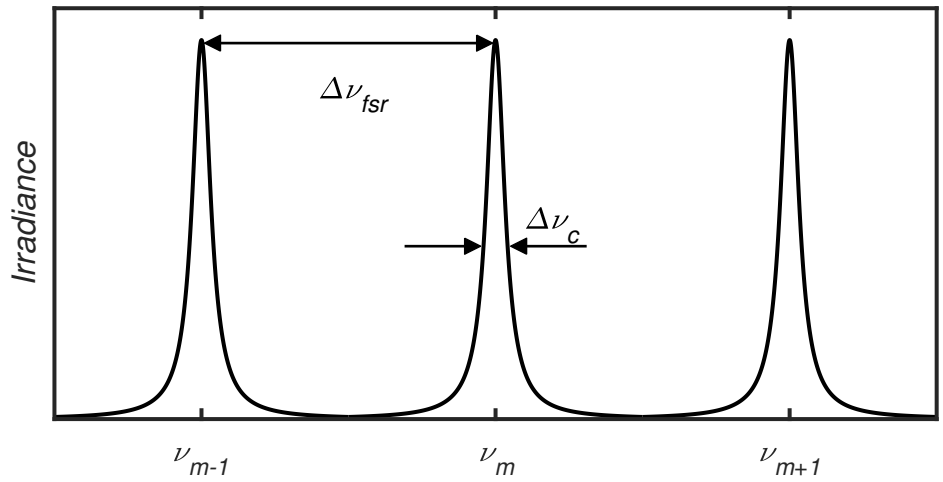

Figure 3.2. *The spectral properties of a FP etalon. The mode frequency ν_m, the free spectral range $\Delta\nu_{fsr}$ and the cavity mode linewidth $\Delta\nu_c$ are defined with the cavity parameters shown in Figure 3.1.*

We can now introduce a cavity quantity called *quality factor*, or Q-factor, which describes the energy storage capability of an optical resonator. Q-factor is formally defined as

$$Q = 2\pi\frac{\textit{energy stored}}{\textit{energy loss during a single pass}}. \tag{3.9}$$

For a certain frequency ν, and wavelength λ, Q-factor can be written in terms of cavity photon lifetime and cavity linewidth using

$$Q = 2\pi\nu\tau_c = \frac{\nu}{\Delta\nu_c} = \frac{\lambda}{\Delta\lambda}, \tag{3.10}$$

which with Equations (3.6) and (3.7) connects Q-factor to the cavity parameters.[9] For laser cavities, typical Q-factors can be on the order of 10^6–10^8. For example, with typical cavity parameters $R_1 = 0.99$, $R_2 = 0.95$ and $L = 10$ cm, we get Q-factor of $\sim 4\times10^7$.

3.1.1 Distributed Bragg Reflector Cavities

Traditional cavity lengths in laser systems and nonlinear optical devices vary from centimeters to few meters, making them incompatible for micro-scale devices [3, 9]. Fortunately, use of layered thin film structures such as distributed Bragg reflector (DBR) cavities has decreased the sizes of optical systems down to millimeters [42–44]. Therefore, DBR cavities are often used in semiconductor lasers and other photonic integration applications.[45–48].

DBRs are periodic structures designed to reflect wavelengths close to a target wavelength λ_B. As Figure 3.3(a) shows, one DBR grating period consists of a pair of layers of high and low refractive index materials.[45] In order to achieve high reflectance at λ_B, the length of one grating period Λ must uphold the *Bragg condition*

$$m\lambda_B = 2n_{eff}\Lambda, \tag{3.11}$$

where n_{eff} is the effective refractive index of the grating and m is an integer [42].

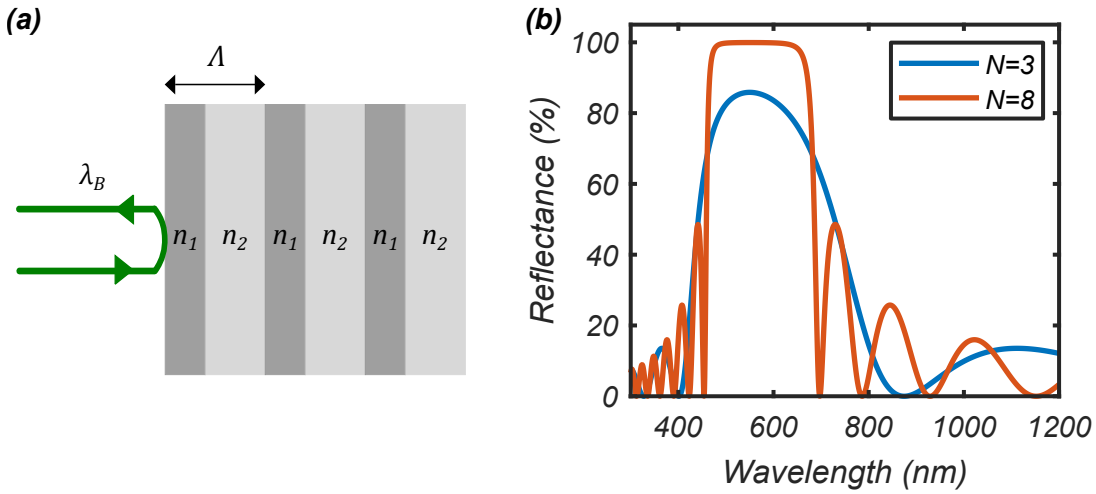

Figure 3.3. ***(a)*** *A schematic drawing and* ***(b)*** *reflectance spectrum of distributed Bragg reflector designed to reflect the wavelength $\lambda_B = 550$ nm. The grating is constructed with titanium dioxide (TiO_2, $n_1 = 2.5$) and silicon dioxide (SiO_2, $n_2 = 1.45$) resulting in a grating period $\Lambda \approx 150$ nm. For grating of eight layer pairs, reflectance band has a clean top-hat profile (red line) around λ_B while with three layer pairs (blue line) relfectance is lower and the band profile deformed. Here, the material dispersion is neglected.*

The Bragg condition is typically fulfilled by setting layer thicknesses to an integer multiplier of $\lambda_B/4$. Then, the reflectance of DBR can be accurately estimated by using equation [45]

$$R = \frac{1 - (n_1/n_2)^{2N} n_1^2/n_0^2}{1 + (n_1/n_2)^{2N} n_1^2/n_0^2}, \tag{3.12}$$

where n_1 and n_2 are refractive indices of high index and low index materials, respectively, n_0 is the refractive index of the surrounding medium, and N is the number of the layer pairs.

From Equation (3.12) follows that R increases with N, and also with the quantity $\Delta n = |n_1 - n_2|$. Thus, with large Δn fewer layers are required for high reflectance values. It is noticeable though, that larger Δn leads to a wider reflection band structure and stronger sidebands [45]. The sidebands can be reduced with several methods such as chirping or apodization of the grating [49]. These methods are worth of consideration when fabricating DBRs but are however beyond the scope of this Thesis.

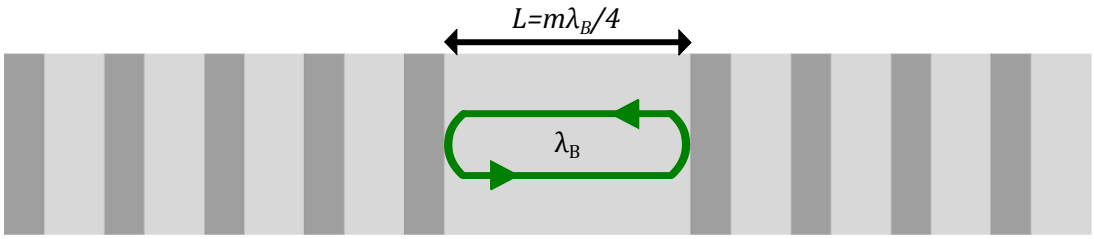

Figure 3.4. *A schematic drawing of a FP etalon formed with two distributed Bragg reflectors separated by distance L. The etalon is designed to operate around the Bragg wavelength λ_B which requires that L must be an integer multiplier of $\lambda_B/4$.*

As was mentioned earlier, DBRs can be used to form sub-wavelength FP etalons, as is demonstrated in Figure 3.4. For DBR cavities, the condition for cavity length is [43, p.219]

$$L = m\frac{\lambda_B}{4}, \tag{3.13}$$

which differs from the previous cavity length condition of Equation (3.2).

In typical applications of DBR cavities, the sizes of DBRs and cavity lengths are of the order of few millimeters [43]. As Equations (3.4), (3.10) and (3.12) imply, this leads to extremely high Q-factors ($Q \sim 10^8$) for such cavities. However, Q-factor of around a few thousands is quite adequate for our research. This enables the use of DBR cavities with dimension of the order of few micrometers in this Thesis.

3.2 Optical Parametric Oscillator

Next, we describe an application of optical cavities and nonlinear optics called *optical parametric oscillators* (OPOs). As Figure 3.5 illustrates, the two main components of an OPO are the nonlinear crystal and the optical cavity around it. The phase-matched DFG in the crystal and the mode-locking capabilities of the cavity result in an efficient conversion of pump frequency ω_p to signal frequency ω_s, and sometimes also to idler frequency ω_i.[3] of [3].

As was mentioned earlier, the frequency conversion in OPO is achieved with DFG. For crystal length of a few millimeters, efficient DFG requires phase matching throughout the crystal. Similar to SHG (see Equation (2.68)), phase matching is dependent on wavevec-

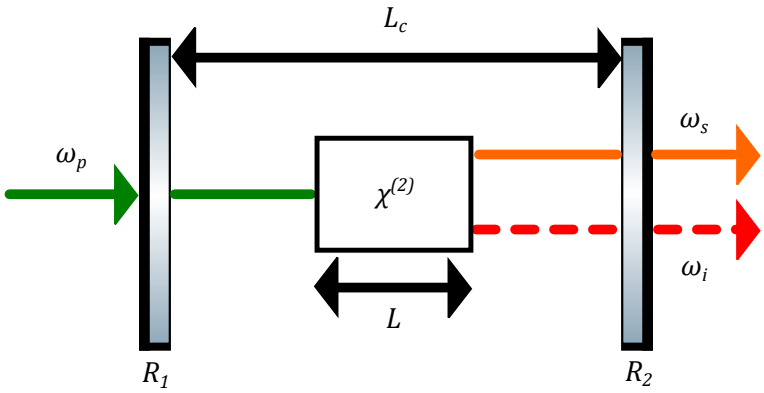

Figure 3.5. *A schematic drawing an OPO. A nonlinear crystal with length L and second-order susceptibility $\chi^{(2)}$ is inserted into an optical cavity. The cavity has length L_c and mirror reflectances R_1 and R_2. OPO is pumped with a pump frequency ω_p which generates an idler frequency ω_i and a signal frequency ω_s, via the process of DFG.*

tor mismatch Δk which we write for DFG as [3]

$$\Delta k = k_i - k_s - k_p, \tag{3.14}$$

where propagation constants k_i, k_s and k_p are defined by Equation (2.69).

Let us now assume a phase-matched crystal in which frequency conversion is relatively efficient for a frequency band $\Delta\omega_s$, also known as the gain linewidth of the nonlinear medium. The crystal is now placed between two mirrors with high reflectances, resulting in a laser cavity of sorts with a nonlinear gain medium. As is shown in Figure 3.6, $\Delta\omega_s$ is much larger than the linewidth $\Delta\nu_c$ and the free spectral range $\Delta\nu_{fsr}$ of the cavity. Thus, there are several values for ω_s with high enough material gain that can be coupled into the cavity. However, only the ω_s closest to the perfect phase-matching condition, i.e. $\Delta k = 0$, is strongly enhanced and is selected as the output frequency. As the cavity mode frequencies depend on the cavity, ω_s can be accurately tuned by changing the cavity length.[3]

OPOs are widely used as tunable laser sources in ultraviolet, visible and infrared regions. They are used to produce nano-, pico- and femtosecond laser pulses as well as continuous-wave lasers. [50, 51] In this Thesis, however, we are not using an OPO as a light source. We are more interested in the operating principles of an OPO which we will apply to some extent in our sample design.

3.3 Metasurfaces

Metamaterials are artificial materials consisting of nanoscale structures such as metal nanoparticles or dielectric gratings. They can exhibit optical properties that are not found in nature such as strong optical activity, epsilon-near-zero behaviour, nano-scale phase-engineering, and magnetism at optical frequencies [10–15]. Due to the growing demand

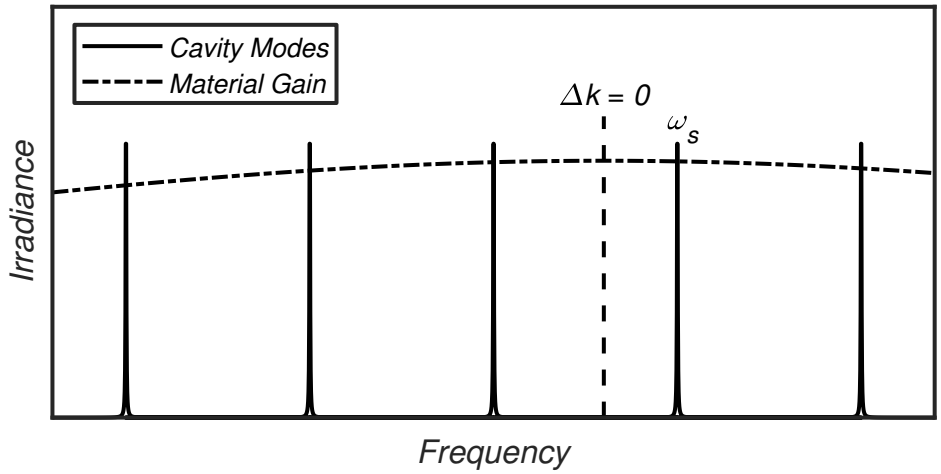

Figure 3.6. *The spectral profiles of the material gain of the nonlinear material (dotted line) and the optical cavity (solid line) of an OPO. The cavity mode frequency that is closest to the perfect phase-matching condition ($\Delta k = 0$, dashed line) is selected as the signal frequency ω_s.*

for miniaturization of nonlinear photonic devices, numerous studies have investigated also the nonlinear properties of metamaterials. [18, 20, 21, 26, 27, 52].

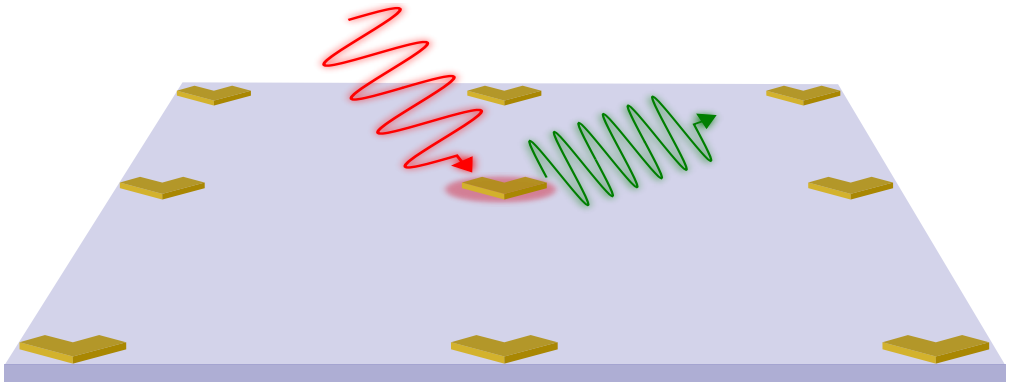

Figure 3.7. *A plasmonic metasurface consisting of L-shaped metal nanoparticles. The metasurface is designed to convert fundamental frequency (red wave) to doubled frequency (green wave) via SHG.*

Metamaterials may consist of only one layer of nanostructures, in which case they are often called *metasurfaces*. Here, we focus on *plasmonic metasurfaces* consisting of L-shaped metal nanoparticles (NPs), illustrated in Figure 3.7. The L-shape was selected to fulfill the symmetry requirements of SHG, which has been experimentally verified in the past [22, 53]. We start with a description of the material response of a single NP called *localized surface plasmon resonance* (LSPR). Then, we describe the response of a periodic lattice of metal nanoparticles called *surface lattice resonance* (SLR). Both resonances can be used to couple light into metasurfaces. From this point of view, metasurfaces can be thought to act as an optical resonator.

3.3.1 Localized Surface Plasmon Resonance

The optical properties of metals are governed by their electronic structure. The most common model to understand the properties of metals is *the free electron gas model* where valence electrons are assumed to move freely between positively charged metal ions [54]. Therefore, metals to conduct heat and electric charge better than most solids, and due to this fact these electron are called *conduction electrons*. When a metal is illuminated with light, the electromagnetic interactions induce oscillations in the conduction electrons. The oscillations are called *plasmons*, and they have a specific frequency called *plasmon frequency*. When the incident light and plasmons are in resonance, the light is coupled into the metal structure causing an electronic excitation. In NPs, the excitation is restricted to the particle dimensions, and thus the particle exerts an effective restoring force on the oscillating particles which enhances the local electric field near the particle. This resonance is LSPR and it occurs at the resonance wavelength λ_0. [36]

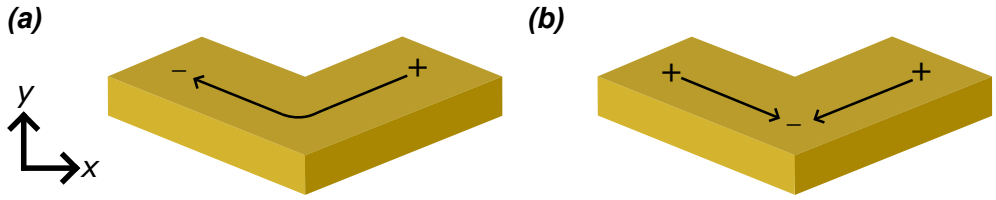

Figure 3.8. *The current distributions associated with effective electric dipoles in an L-shaped metal nanoparticle for* ***(a)*** *x-polarized and* ***(b)*** *y-polarized incident light [23]. The associated local fields give rise to LSPRs. Here, the resonance wavelength is longer for x-polarized than for y-polarized light.*

The spectral location of LSPR, i.e. value of λ_0 depends on many parameters. First of all, the choice of material affects λ_0 significantly. For example, silver has typically shorter resonance wavelength than gold [55]. Second, the particle size impacts as well, as λ_0 increases monotonically with particle dimensions. Connected to the previous, the polarization of the incident light also has an impact on λ_0. The induced dipoles are parallel to the incident polarization, and thus the resulting electric current follows a path in the particle that connects the two poles of the induced dipole (marked with black arrows in Figure 3.8). Now, λ_0 increases with the length of the mentioned path. Therefore for L-shaped NPs, λ_0 is larger for the x-polarized incident light than for the y-polarized incident light. Finally, the refractive index of the surrounding medium and the neighbouring NPs also have a shifting impact on λ_0.[36] The inter-particle coupling of plasmons can also impact the resonance linewidth, as was demonstrated by Czaplicki et al. [27]. Next, we will describe the impact of the efficient inter-particle coupling in a periodic metasurface illustrated in Figure 3.9.

3.3.2 Surface Lattice Resonance

When NPs are organized in a periodic lattice, they act as a diffraction grating. The incident light is then diffracted from the grating in accordance with equation [25]

$$n_{sub}\sin(\beta_i) = n_{sup}\sin(\theta) \pm i\lambda p, \tag{3.15}$$

where i is the diffraction order, λ is the wavelength of the incident beam, p is the grating period, θ is the incident angle, and n_{sub} and n_{sup} are the refractive indices of transmitted (substrate) and incident (superstrate) medium, respectively. In typical experiments, the tuned θ is the incident angle in air. Then, according to Snell's law, we can set $n_{sup} = 1$ even if the grating is covered with a superstrate material.

At a certain wavelength or a certain incident angle, the diffracted wave starts to propagate along the grating surface, i.e. $\beta_i = 90°$. Then, the induced dipoles in NPs start to couple efficiently giving a rise to a collective response known as a SLR. The spectral features of SLRs, also known as Rayleigh anomalies, can be extremely narrow and sensitive which makes them ideal for e.g.sensing applications. Furthermore, the grating material itself does not impact the diffraction from the grating. Thus, also fully dielectric structures exhibit resonances similar to SLRs that are called *guided-mode resonances* (GMR) [56–59].

We can now rewrite Equation (3.15) and derive an equation for the spectral location of a SLR as [60]

$$\lambda_i = p\left(\frac{n_{sub}}{|i|} - \frac{\sin(\theta)}{i}\right). \tag{3.16}$$

It is worth mentioning that SLRs arise only if the incident light is polarized *perpendicular* to the grating period. As much is illustrated in Figure 3.9 where two SLR modes of a plasmonic metasurface propagate in the direction perpendicular to their polarization.

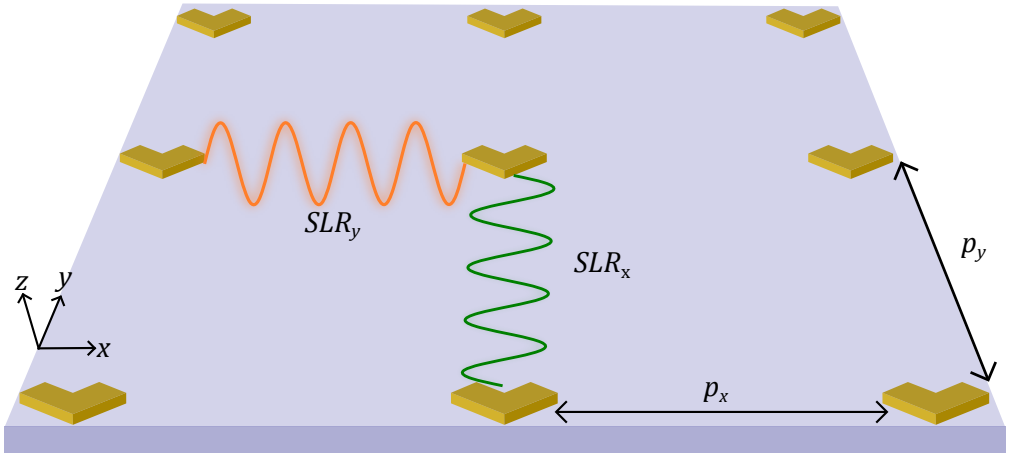

Figure 3.9. *Surface lattice resonance modes for a periodic plasmonic metasurface. When light is polarized along either x- or y-coordinate, the resonance wavelengths depend on the lattice constant (p_y or p_x) perpendicular to the polarization.*

We have now introduced two typical resonances of periodic plasmonic metasurfaces, LSPR and SLR. They both have been successfully used as to enhance and engineer linear and nonlinear optical processes alike. However, the coupling efficiency has a substantial difference between the two resonances. As is shown in Figure 3.10, the Q-factor of a SLR can be as high as a few thousand but for LSPR Q-factor is usually remarkably lower ($Q < 10$). The low Q-factor indicates the high losses of LSPR, which also explains the high heating impact of the resonance, and thus the low damage thresholds of metal nanoparticles. With this remark, SLRs with high Q-factors seem superior for any applications that require strong electric fields, such as nonlinear processes.

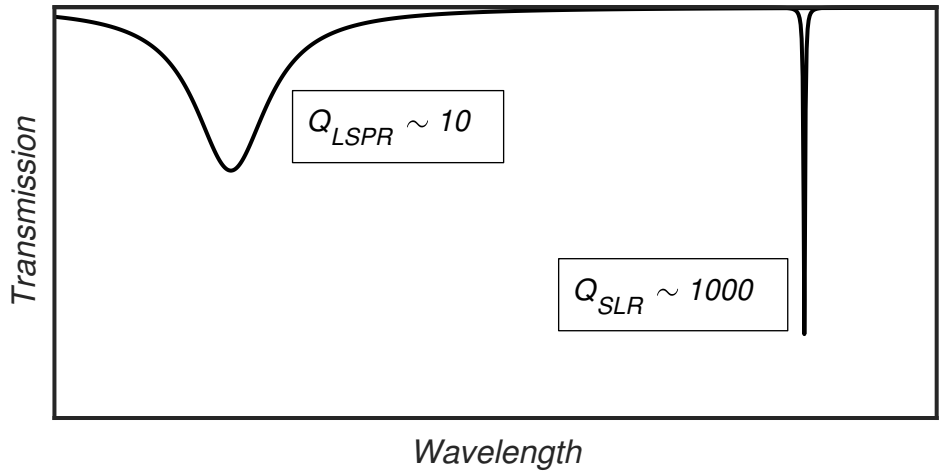

Figure 3.10. *An illustrative transmission spectrum of a periodic metasurface with resonance peaks and Q-factors for localized surface plasmon resonance (LSPR) and surface lattice resonance (SLR).*

When designing an SLR-exhibiting metasurface, it is worth recalling that LSPR and SLR can impact each other. If LSPR and SLR resonance wavelengths are close to each other, their resonance lineshapes are distorted: LSPR becomes a Fano-type resonance with narrowed linewidth, and SLR linewidth increases significantly [27]. To avoid this problem, it is beneficial to design these two resonances adequately apart from each other.

3.4 Second-harmonic Generation from Metasurfaces

In this section, we outlay the basic principles of SHG from plasmonic metasurfaces. As is shown in Figure 3.8, the L-shaped particles have only one symmetry axis coinciding with the y-axis of the surface coordinate system. When the particles are organized in a rectangular lattice, the metasurface belongs to the point group C_{3v} [61]. When incident light propagates along the z-axis, we have only three independent non-zero second-order tensor components: $\chi^{(2)}_{yyy}$, $\chi^{(2)}_{yxx}$, and $\chi^{(2)}_{xxy}(=\chi^{(2)}_{xyx})$ [3].

Traditionally, SHG is enhanced with *singly-resonant* metasurfaces where LSPR coincides with the fundamental wavelength [22, 23, 26, 53]. This creates strong local electric fields at fundamental frequencies enhancing the SH-signal in agreement with the local-field

model described in Section 2.9. The singly-resonant use of SLR has also been experimentally demonstrated for dielectric and plasmonic metamaterials alike [19, 62]. In the latter, the SH-enhancement is far greater with SLRs than with LSPRs, when compared to the off-resonance signal. When we compare the linewidths of these two resonances and consider the Miller's rule (2.53), this result is quite expected.

An experimental study performed by Celebrano et al. [63] shows that SH-signal can be improved even further with *multiresonant* metamaterials. In a multiresonant design, material resonances occur both the fundamental and at the SH-wavelengths which, again following the local-field model, enhances the SH-signal. However, the utilization of multiresonant design requires that the fundamental and SH-fields have orthogonal polarizations which then connects the SH-signal to the tensor component $\chi^{(2)}_{yxx}$. In recent numerical studies [28, 64], Huttunen et al. demonstrate multiresonant sample designs which utilize several SLRs and could achieve reasonable conversion efficiencies with second- and third-order processes.

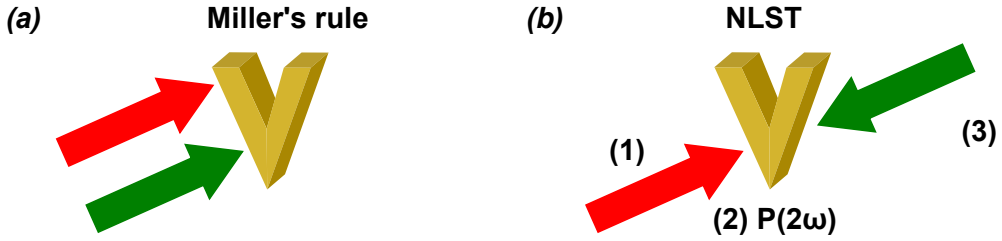

Figure 3.11. *Two methods to evaluate the nonlinear response of plasmonic metasurfaces.* ***(a)*** *Miller's rule consists of evaluation of the linear properties at fundamental and second-harmonic wavelengths.* ***(b)*** *Nonlinear scattering theory (NLST) has three evaluation steps:* ***(1)*** *The excitation by the fundamental field;* ***(2)*** *calculation of SH-polarization; and* ***(3)*** *the evaluation of the overlap integral between the SH-polarization and the local-field induced by a wave propagating from the detector and oscillating at the SH-frequency.*

Even though the Miller's rule predicts correctly superiority of SLR over LSPR, it is not accurate enough to describe nonlinear responses of metasurfaces [65, 66]. Instead, the *nonlinear scattering theory* (NLST) [67], illustrated in Figure 3.11, should be used. NLST evaluates the SH-emission $E_{nl}(2\omega)$ with three steps. The first step is the material excitation by the fundamental field. The second step is the calculation of the SH-polarization. As a final step, we evaluate the overlap integral be between SH-polarization and the local-field induced by a wave propagating from the detector and oscillating at the SH-frequency. Then, the SH-emission is evaluated by using the following overlap integral:

$$E_{nl}(2\omega) \propto \iint \chi^{(2)} E^2(\omega) E(2\omega) dS, \tag{3.17}$$

where dS indicates the integration over the metasurface. $E(\omega)$ and $E(2\omega)$ are dependent on the local-fields at the fundamental and SH frequencies, respectively.

4 RESONANT WAVEGUIDE GRATINGS

In this chapter, we demonstrate proof-of-principle studies performed on fully dielectric resonant waveguide gratings (RWGs) made from silicon nitride (SiN). We start with a description of our samples and measurement conditions. Then, we will describe the experimental setup used for the linear and nonlinear measurements. Next, we will explain the simulation methods used to estimate the second-harmonic response of our RWGs. In the second and third sections, we demonstrate a clear agreement between our simulations and experiments. We start by comparing the simulated and measured linear properties of our RWGs. Then, we present our results for the measured and simulated SH emission from our samples. We conclude this chapter with the evaluation of our simulation methods and with some proposals for future studies.

4.1 Samples and Research Methods

The RWGs studied here consisted of SiN. We used ion-beam-sputtering (IBS) [68] to fabricate 90–100 nm thick SiN gratings ($n_g = 1.9$) on fused silica ($n_s = 1.457$) and to cover them with silicon dioxide (SiO_2 , $n_c = 1.49$). Here, we set the grating periods p of our samples to 500 and 600 nm and labelled them accordingly as S500 and S600. The widths of the SiN grooves in the RWGs were half of the grating period, and thus, both samples had the same amount of active material (SiN). The differences in optical properties should then be a consequence of the different grating periods. An illustrative drawing of a SiN RWG is shown in Figure 4.1.

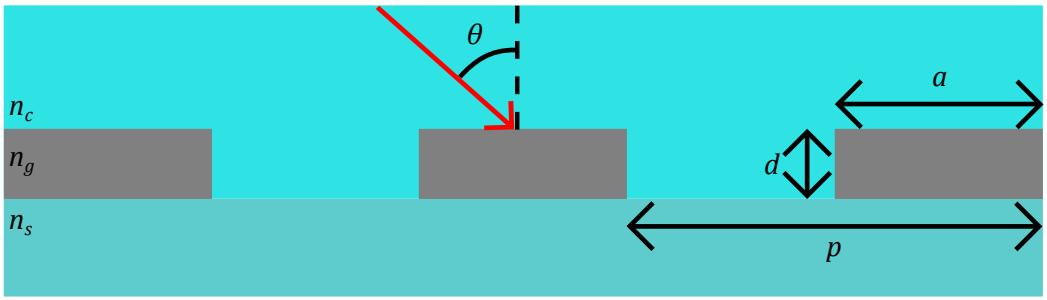

Figure 4.1. *Schematic drawing of a resonant waveguide grating made of silicon nitride (SiN, $n_g = 1.9$). The gratings are fabricated on fused silica ($n_s = 1.457$) and covered with a silicon dioxide cladding (SiO_2, $n_c = 1.49$). SiN lines have thickness $d = 90-100$ nm, and width a which is half of the grating period p. The grating is illuminated with laser light centered at wavelength $\lambda = 1064$ nm at an incident angle θ.*

As is shown in Figure 4.1, our RWGs are centrosymmetric. In order to fulfill the symmetry requirements for SHG, the incident angle θ had to be tuned. The tuning of the incident angle helps us to efficiently excite GMRs, as they are also angle dependent (see Equation (3.16)). Now, it is useful to rewrite Equation (3.16) for the first-order ($i = \pm 1$) resonance angles as

$$\theta_{\pm 1} = \operatorname{asin}\left(\pm\left(n_s - \frac{\lambda}{p}\right)\right), \tag{4.1}$$

where wavelength λ is set to 1064 nm. In this case, the first-order RAs appear at the incident angles of 42.5° and 18.6° for $p = 500$ nm and 600 nm, respectively. The wavelength–angle correspondence for the first-order RAs is illustrated in Figure 4.2.

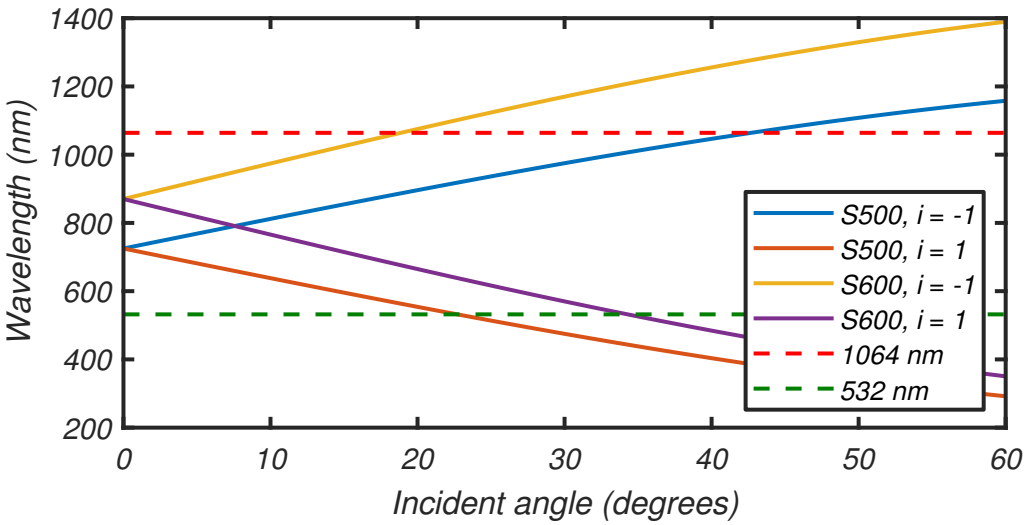

Figure 4.2. *The resonance wavelength as the function of the incident angle for the first-order RAs. For fundamental wavelength of 1064 nm (red dashed line), the RA angles of order i = –1 are 42.5° and 18.6° for samples S500 and S600, respectively. The corresponding angles for RAs of order i = 1 at SH wavelength of 532 nm (green dashed line) are 22.7° and 34.2°.*

In order to measure the transmittance and SH response of our RWGs, we used the setup illustrated in Figure 4.3. As a light source, we used a pulsed Nd:YAG (Ekspla PL 2200) laser with a wavelength of 1064 nm, pulse duration of 60 ps and a repetition rate of 1 kHz. To avoid possible sample damage, we limited the input power of the laser to 3 mW with a half-wave plate (HWP) and a linear polarizer (LP). In order to efficiently excite GMRs, we then used another HWP to set the polarization along the SiN lines of the RWGs. Then, another LP was used to select the correct polarization of the generated SH signal. To ensure efficient coupling to the GMR modes, the laser beam as weakly focused on the sample using a lens with a focal length $f = 400$ mm. The sample itself was placed on a rotating stage allowing us to measure the transmittance and the SHG as the functions of the incident angle. Furthermore, we put the sample between a long-pass filter (LPF) and a short-pass filter (SPF). This ensured that the detected SHG emission was only due to the sample emission. As the SH responses of nanoscale structures are typically very weak, we used a photomultiplier tube (PMT) to detect the SH signal. In linear measurements, we turned LPF aside and used a photodiode to measure transmission of the

fundamental wavelength 1064 nm.

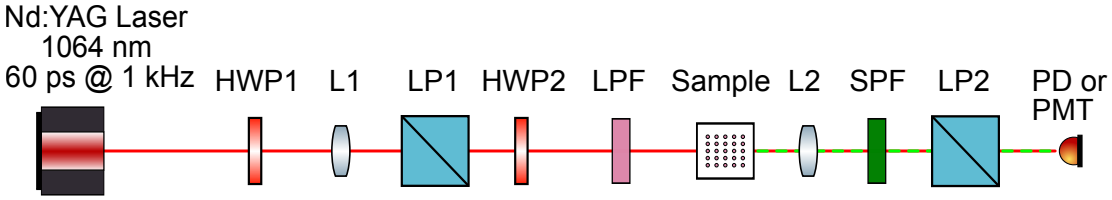

Figure 4.3. *Schematic drawing of the experimental setup. The focal lengths of the lenses are 400 mm (L1) and 50 mm (L2). HWP = Half-wave plate, LP = Linear polarizer, LPF = Long-pass filter and SPF = Short-pass filter. The sample was put on a rotating stage allowing us to change the incident angle. In the nonlinear measurements, the SH signal was collected using a photomultiplier tube (PMT). In linear measurements, SPF was turned aside and the transmission was measured with a photodiode (PD).*

In order to connect the nonlinear scattering theory (NLST) to the experiments, we also performed numerical simulations based on our RWGs. We performed the first part of our simulations using a commercial *Lumerical FDTD Solutions* software which uses the finite-domain time-domain (FDTD) [69] method to evaluate electromagnetic fields present in the structure. We performed two-dimensional simulations for a structure illustrated in Figure 4.1. As an excitation source in our simulations, we used a plane wave with a wavelength of 1064 nm which we polarized along the SiN grooves. To gather the required data for the calculation based on the NLST, we used three monitors in our simulation system. One monitor measured transmission T of fundamental light.The other two measured electric field profiles E_{fund} and E_{SH} near the SiN gratings at the fundamental and SH wavelengths, respectively. By performing an angle sweep, we gained values for T, E_{fund} and E_{SH} as the functions of the incident angle θ. Then, we inserted the gained field profiles to Equation (3.17) and got an estimation for the scattered SH field. By then transforming the scattered SH field into irradiance we were able to compare the numerical predictions with the experimental results.

4.2 Linear Properties

We investigated the linear and nonlinear optical properties of SiN RWGs with two different grating periods ($p = 500$ and 600 nm). First, we measured and simulated the transmission of the fundamental wavelength 1064 nm as a function of the incident angle θ. As is shown in Figure 4.4, we performed experiments over the range $\theta = 0°–50°$ but we limited the simulation range closer to the theoretical RA angles given by Equation (4.1).

The first glance at Figure 4.4 reveals that the simulations and experiments agree rather accurately on the angular locations of the GMRs. The small differences between theoretical and experimental values can be plausibly explained by the uncertainties associated with the experimental setup. It is also worth mentioning that all resonances correspond to the diffraction order $i = –1$ and that the resonance angles θ_{exp} and θ_{sim} decrease with p.

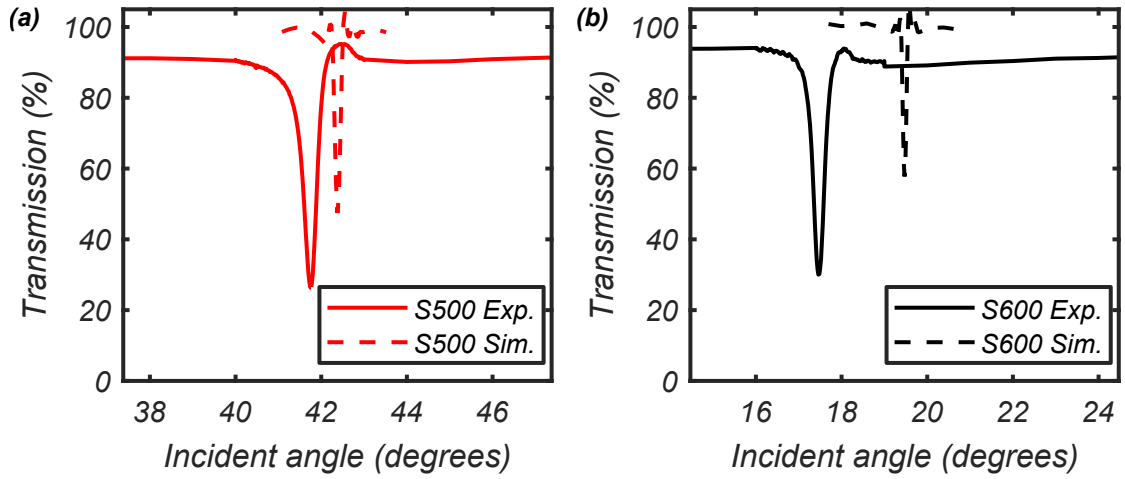

Figure 4.4. *Experimental (solid lines) and simulated (dashed lines) transmission as function of incident angle for samples* ***(a)*** *S500 (red)* ***(b)*** *and S600 (black). The resonance angles are around 18 °and 42 °for S500 and S600, respectively.*

Another difference between the experimental and simulated results is in the strengths of the resonance peaks. The experimental peaks have practically equal amplitudes, which is a rather expected result since both samples have the same amount of SiN. The simulated transmission peaks, however, have slightly different amplitudes for our samples. It is then likely that our simulations did not cover the most optimal coupling conditions. This implies that the spectral simulation resolution was slightly inadequate, especially in the simulation for S600. However, improving the simulation conditions is quite time consuming and would, in the end, lead to results with spectral features much narrower than those of the light sources and fabricated samples used in experimental work.

The mere locations and strengths of the resonance peaks do not offer much information that is needed to evaluate the nonlinear properties of our samples. The angular linewidths $\Delta\theta_{sim}$ and $\Delta\theta_{exp}$ are more relevant since they are connected to the *spectral linewidth* by equation

$$\Delta\lambda = p\cos(\theta)\Delta\theta, \tag{4.2}$$

and thus, also to the Q-factor through Equation (3.10). As the emitted SH irradiance scales as $I_{SHG} \propto Q^4$, angular linewidths help us to estimate the SH responses of our samples. The relevant results of our linear experiments are listed in Table 4.1.

Table 4.1. *Linear results for samples S500 and S600. The angle θ_{RA} is the theoretical incident angle of the Rayleigh anomaly, and θ_{sim} and θ_{exp} are the simulated and experimental resonance angles, respectively. $\Delta\theta_{sim}$ and $\Delta\theta_{exp}$ are the angular linewidths and Q_{sim} and Q_{exp} are the Q-factors of the simulated and measured resonances, respectively.*

Sample	θ_{RA}	θ_{sim}	θ_{exp}	$\Delta\theta_{sim}$	$\Delta\theta_{exp}$	Q_{sim}	Q_{exp}
S500	42.5°	42.4°	41.7°	0.1°	0.4°	1650	410
S600	18.6°	19.5°	17.5°	0.1°	0.3°	1080	350

The experimental linewidths $\Delta\theta_{exp}$ are significantly larger than their simulated counterparts $\Delta\theta_{sim}$. This is most likely a consequence of the differences between the light sources used in simulations and experiments. In the simulations, the light source is a perfect plane wave without divergence, while the laser beam used in the experiments has a slight divergence. The experimental Q-factors are thus reduced when compared with the Q-factors of the simulation results. When we compare these results against the predictions based on the Miller's rule, the GMR-enhanced SHG would be stronger for S500 based on experiments and simulations alike. Since the SH emission scales as $I_{SHG} \propto Q^4$, the experimental Q-factors now imply that S500 should have three times stronger SH response than S600. Alternatively, based on simulated Q-factors, the SH-response of S500 should be seven-fold to the response of S600.

4.3 Second-harmonic Generation from Resonant Waveguide Gratings

Next, we studied the SH response of our samples using the setup shown in Figure 4.3. We performed measurements over incident angles $\theta = 0° - 70°$ and obtained the results plotted in Figure 4.5. The values for the emitted SH power shown in the graph are rough estimations due to the inaccuracies of our detection devices. First, the noise levels of our PMT might vary significantly between the measurements. Moreover, the power meter used for power calibration had a noise level of the order of 10 fW. Combined, these inaccuracies result in error terms up to 30 fW for our experiments. Nevertheless, the order-of-magnitude should be correct, and thus we estimate conversion factors on the order of 10^{-11} for both samples.

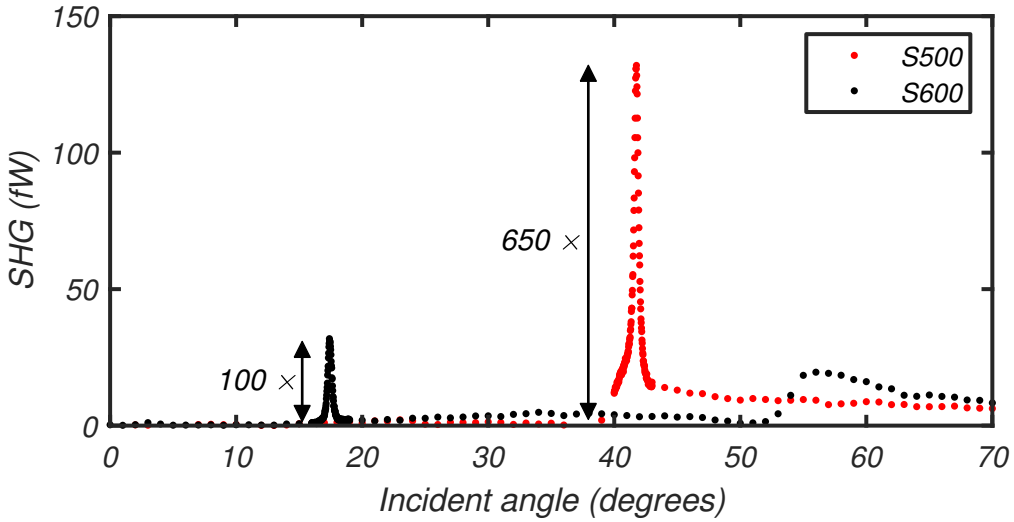

Figure 4.5. *Measured SH power as a function of incident angle for samples S500 (red) and S600 (black). The strongest signals are measured at the experimental resonance angles defined in the transmission measurements. The resonance enhancement compared with the off-resonance signals are 650 and 100 for S500 and S600, respectively.*

The results shown in Figure 4.5 further confirm that the GMRs enhance the local fields present in the SiN RWG. coincide well with the measured resonance angles, and are deviated only by around 0.1°. The linewidths of the SH peaks are also equal to the linewidths $\Delta\theta_{exp}$ of the SLR peaks. As was expected based on the measured Q-factors, S500 has a SH response that is roughly four times stronger than the emitted SH power of S600. However, this relation may be inaccurate since the absolute values for the emitted power may slightly vary between separate measurements. Another, and possibly more accurate method to evaluate the role of the resonance enhancement would be to compare the resonant signals with the off-resonance signals, illustrated with double arrows in Figure 4.5. These enhancements are 650 and 100 for S500 and S600, respectively. This result agrees rather well with the simulated Q-factors based on which we estimated a seven-fold difference between the two samples. Considering the results so far, we conclude that the simulations define the linear properties accurately.

In order to validate the NLST method as a reliable basis for simulation, we need to consider our results beyond the simulated Q-factors. The incident light induces dipole moments into the SiN grating that are then amplified by the propagating GMR mode. This gives rise to the local fields at the fundamental wavelength, and according to NLST, also to the SH emission. As is shown in Figure 4.6, the local field has a 12-fold increase at the resonance angle (42.4° for S500) when compared with the off-resonance electric field. For S600, the local-field enhancement is roughly ten-fold and occurs at the simulated resonance angle 19.5°. For the vacuum field term in Equation (3.17), we also simulated local fields at the SH wavelength. As the first-order RA-angles for $\lambda = 1064$ nm and $\lambda = 532$ nm differ quite significantly for both of our samples (see Figure 4.2), the local field at $\lambda = 532$ nm remains constant over the simulated angles.

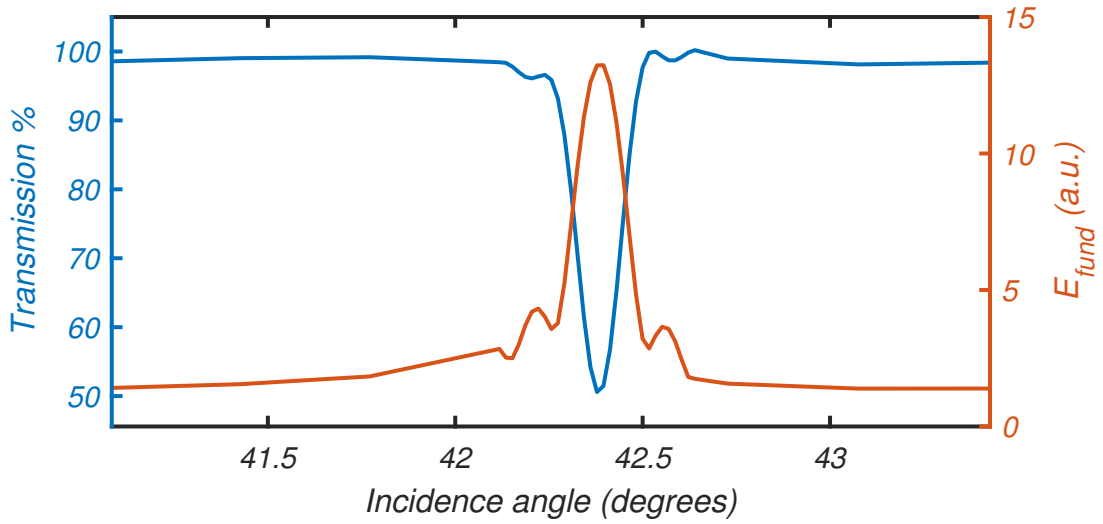

Figure 4.6. *Simulated transmission and the local electric field E_{fund} for the sample S500. The local electric field is normalized to the field amplitude next to the resonance. At the resonance angle 42.4°, the local field is 14-fold when compared with the off-resonance field.*

Next, we inserted the gained field profiles at the fundamental and SH wavelength to

the Equation (3.17). From there, we obtained simulated angle-dependence for the SH power emitted from our RWG structures. For visual comparison between simulated and experimental results, shown in Figure 4.7, we normalized all data sets to the maximum value of each individual set. We can then compare the resonance enhancements and peak locations of simulation with the experimental results.

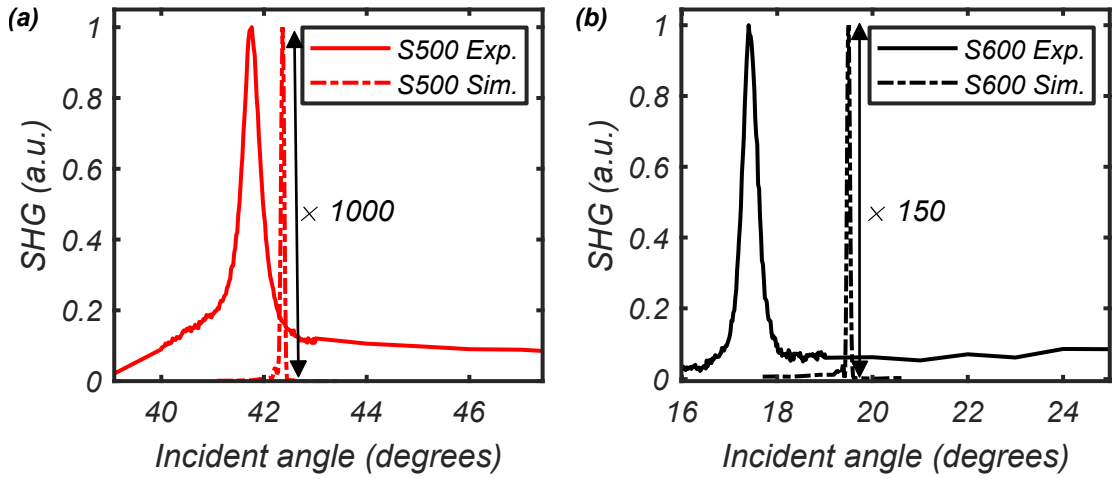

Figure 4.7. *Emitted SHG signal based on the experiments (solid lines) and simulations (dashed lines) for samples* ***(a)*** *S500 and* ***(b)*** *S600. The signal enhancements compared to the off-resonant values are 1000 and 150 for S500 nm and S600, respectively. All data sets are normalized to the maximum signal of each individual set. Thus, the graphs do not display information about the signal strengths relative to the other sets.*

For both samples, the simulated SH emission peaks locate at the same incident angles and have the same linewidths than the corresponding GMR peaks. This further confirms the role of GMR as an effective field-enhancing response. Also, the simulated resonance enhancement factors agree with the experimental results. Once again, the enhancement factor of S500 is seven-fold to the factor of S600. This agrees with the Q-factor-based estimation we made in Section 4.2. Relevant results from SHG measurements and simulations are listed in Table 4.2.

Table 4.2. *Nonlinear results for samples S500 and S600. The SH emission peaks locate at the incident angles θ_{sim} and θ_{exp} for simulations experiments, respectively. They have angular linewidths $\Delta\theta_{sim}$ and $\Delta\theta_{exp}$. At these resonant angles, the SH emission is enhanced by factors E_{sim} and E_{exp} in simulations and experiments, respectively.*

Sample	θ_{sim}	θ_{exp}	$\Delta\theta_{sim}$	$\Delta\theta_{exp}$	E_{sim}	E_{exp}
S500	42.4°	41.7°	0.1°	0.4°	1000	650
S600	19.5°	17.5°	0.1°	0.3°	150	100

Overall, our results confirm the reliability of FDTD and NLST as simulation methods. Both linear and nonlinear simulations agree with experimental results with adequate accuracy. The differences between the experiments and simulations can be explained with the uncertainties associated with our experimental setup and with the limitations of our simulations. For example, by improving the collimation of our laser beam, we should reach better agreement between the experimental and simulated results.

More importantly, our results validate utilizing GMRs as an effective method to engineer and enhance the SHG in dielectric materials. Our results motivate to design fully dielectric structures suitable for other nonlinear processes such as SPDC, DFG, and cascade third-harmonic generation. The processes could be used to realize nanoscale photon-pair generation and light sources opertaing in THz and ultraviolet regions.

5 RESONANT PLASMONIC METAMATERIALS

In this chapter, we propose two novel plasmonic metamaterials designed to emit coherent photon pairs via SPDC. For both designs, the building blocks are L-shaped aluminum nanoparticles placed in a homogeneous dielectric medium, such as in glass. The first sample is a multiresonant metasurface exhibiting SLRs both at the pump and the signal wavelengths for orthogonal polarizations. The second sample consists of a singly-resonant metasurface sandwiched between two distributed Bragg reflectors. In this sample, the multiresonant conditions are achieved by coupling the pump wavelength to the cavity mode and the signal wavelength to the SLR. For both designs, we used FDTD and NLST in order to evaluate their SPDC-response.

5.1 Simulation Methods

In order to evaluate different enhancement methods, we simulated SPDC-response of two different types of plasmonic metamaterials. Both structures, described in detail later, consisted of L-shaped aluminum nanoparticles embedded in a homogeneous medium ($n_s = 1.45$), visualized in Figure 5.1. The particles had an arm length $L = 90$ nm, an arm width $w = 45$ nm and a thickness $d = 30$ nm. Here, the particle dimensions and the material were chose to exhibit LSPRs at lower wavelengths ($\lambda_{LSPR} \leq 600$ nm). LSPRs would not then interact with the SLR modes, which ensures the high-quality resonances at the pump and signal wavelengths. As in many previous studies [22, 23, 26, 27, 53], the L-shape was selected to fulfill the symmetry requirements of second-order nonlinear processes making $\chi^{(2)}_{yyy}$, $\chi^{(2)}_{yxx}$, and $\chi^{(2)}_{xxy} (= \chi^{(2)}_{xyx})$ the allowed tensor components.

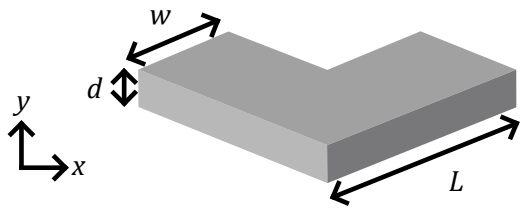

Figure 5.1. *L-shaped aluminum nanoparticle used as a building block in our sample designs. Particle arm length $L = 90$ nm, arm width $w = 45$ nm, and thickness $d = 30$ nm were selected for LSPRs to locate at low enough wavelengths ($\lambda_{LSPR} \leq 600$ nm).*

To evaluate the SPDC response of the sample designs, we used FDTD and NLST in a

very similar manner as already described in Chapter 4. We started by simulating transmission and local fields at pump and signal wavelengths. Unlike in Chapter 4, we had a broadband plane-wave source at the normal incidence polarized first along x-coordinate and then along the y-coordinate of the sample coordinates. We then used NLST to predict the spectral behaviour of SPDC signals corresponding to the tensor components $\chi^{(2)}_{yyy}$, $\chi^{(2)}_{yxx}$, and $\chi^{(2)}_{xxy}(=\chi^{(2)}_{xyx})$. As SPDC and SHG are each other's reverse processes, we could use the same overlap integral as we used in Chapter 4.

5.2 Multiresonant Metasurface

The first sample design, illustrated in Figure 5.2, is a multiresonant metasurface consisting of aluminum nanoparticles as described above. The nanoparticles were arranged in a lattice with lattice periods $p_x = 414$ nm and $p_y = 828$ nm along the $x-$ and $y-$directions in the sample coordinates, respectively. Periods p_x and p_y were selected to give rise to SLRs at the pump wavelength ($\lambda_p = 600$ nm) and signal wavelength ($\lambda_s = 1200$ nm).

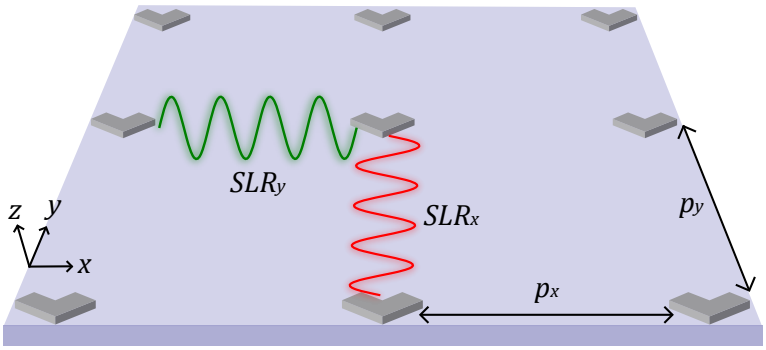

Figure 5.2. *Schematic drawing of a multiresonant metasurface consisting of L-shaped aluminum nanopartilces. Periodicities p_x and p_y are set so that x-polarized SLR is at signal wavelength ($\lambda_{SLR,x} = \lambda_s = 1200$ nm) and y-polarized at pump wavelength ($\lambda_{SLR,y} = \lambda_p = 600$ nm).*

With the selected parameters, the strongest enhancement should occur for the process corresponding to the tensor component $\chi^{(2)}_{yxx}$, i.e. to the process where the pump is $y-$polarized and signal $x-$polarized. Multiresonant design would then mimic type I nonlinear crystals which are widely used in quantum optics [40]. The relevant sample parameters and enhancement methods for multiresonant design are listed in Table 5.1.

Table 5.1. *Metasurface parameters, the designed signal wavelength λ_s, enhancement resonances for pump and signal wavelengths, and optimal tensor components for the multiresonant design. Periods p_x and p_y are the lattice constants in x- and y-coordinates, respectively.*

Sample	λ_s (nm)	p_x (nm)	p_y (nm)	pump resonance	signal resonance	tensors
MR	1200	414	828	SLR_y	SLR_x	yxx

As a start for our evaluation, we simulated the transmission spectra for x- and y-polarized

incident light. The spectra shown in Figure 5.3 confirms the presence of first-order SLRs at the pump ($\lambda_p = 600$ nm) and signal wavelength ($\lambda_s = 1200$ nm) for y-polarized and x-polarized light, respectively. The x-polarized SLR peak has some noise around it which indicates slightly divergent simulations. The other sharp spectral features correspond to the higher-order SLRs, which we will not utilize in this Thesis. The broader spectral features correspond to the LSPRs at 600 nm and 500 nm for x- and y-polarized light, respectively. As was designed, LSPRs do not overlap with the first-order SLRs which confirms that the particle parameters were correctly designed. However, the particles are too small for efficient inter-particle coupling leading to the relatively weak transmission peaks.

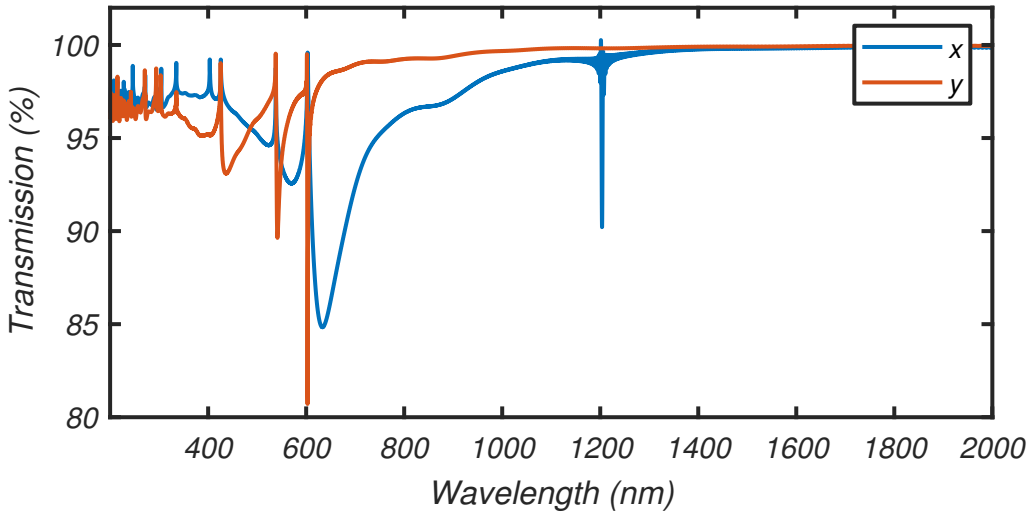

Figure 5.3. *Spectral transmission for the multiresonant sample design. With x-polarized (blue) and y-polarized (red) light, we detect sharp SLR peaks at the signal wavelength $\lambda_s = 1200$ nm and at the pump wavelength $\lambda_p = 600$ nm.*

Yet again, the strengths of the resonance peaks are not the most essential information when considering the nonlinear properties of the designed metasurfaces. Rather the spectral linewidths $\Delta\lambda$ and the corresponding Q-factors are more relevant. From the spectra in Figure 5.3 we observe that $\Delta\lambda$ are roughly 2 nm for both polarizations leading to Q-factors of 430 and 550 for y- and x-polarized light, respectively. For y-polarization, the resonance peak is broadened due to mode coupling with the LSPR. This point illustrates well that it would be difficult to design SLRs to occur at shorter wavelengths than considered here. The LSPRs do not impact the x-polarized resonance peak, but it still has the same linewidth of 2 nm and noise around it due to the before mentioned simulation divergence.

The next step in our simulations was to compute local-field enhancements $E_{loc,p}$ and $E_{loc,s}$ at the pump and signal wavelengths, respectively. As is shown in Figure 5.4, the spectral behaviours of the field profiles confirms that the local fields are considerably enhanced due to SLRs. At the signal wavelength, the local electric field is constant for y-polarized light, while for x-polarized light a strong peak occurs at 1200 nm. Here, one can again see the impact of diverged simulations as small oscillations around the resonance.

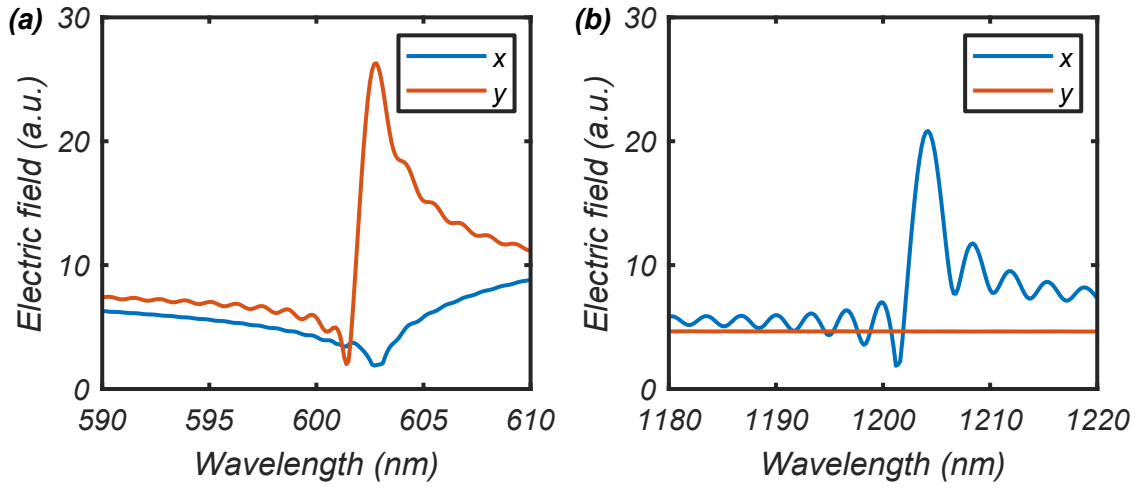

Figure 5.4. *Normalized local electric fields close to the* ***(a)*** *pump wavelength $\lambda_p = 600$ nm and* ***(b)*** *to the signal wavelength $\lambda_s = 1200$ nm. The local fields are SLR-enhanced with y-polarized (red) and x-polarized (blue) incident light at λ_p and λ_s, respectively.*

Close to the pump wavelength, the spectral behaviour of the local field is different. For y-polarized input, a strong resonance peak locates at 600 nm, and the impact of a higher-order SLR is noticeable at the shorter wavelengths. The x-polarized light gives rise to the LSPR at these wavelengths. Consequently, SLR acts as a damping resonance, which can be seen as a dip in the local field at 600 nm.

From the results listed in Table 5.2, we can now predict the SPDC responses corresponding to different tensor components. Based on the Miller's rule and the estimated Q-factors, or by using the NLST method and subsequent local field analysis, $\chi^{(2)}_{yxx}$ should result in the strongest signal of the three components as it utilizes the multiresonant conditions most efficiently. Consequently, the other two should give rise to a much weaker response since they utilize only one of the SLRs.

Table 5.2. *Simulated results for the multiresonant metasurface with x- and y-polarized light sources. The wavelength λ, the linewidth $\Delta\lambda$, and Q-factor for the utilized SLRs. $E_{loc,p}$ and $E_{loc,s}$ are the normalized local field factors at the pump and signal wavelengths, respectively.*

Polarization	λ (nm)	$\Delta\lambda$ (nm)	Q	$E_{loc,p}$	$E_{loc,s}$
y	602.8	1.4	430	26	5
x	1203.8	2.2	550	2	20

As a next step, we used NSLT to evaluate the SPDC response of our metasurface. We calculated the responses over the signal wavelength band of 1180–1220 nm, and studied only the generation of photon pairs with equal wavelengths. The results were normalized to the signal peak of the least efficient process corresponding to $\chi^{(2)}_{xxy} (= \chi^{(2)}_{yxx})$. As was expected based on linear results, and is shown in Figure 5.5, the strongest signal corresponds to $\chi^{(2)}_{yxx}$ and is roughly 400 times stronger than the peak of the weakest signal. The signal corresponding to $\chi^{(2)}_{yyy}$ is only slightly stronger (four-fold) than the one corresponding to $\chi^{(2)}_{xxy}$.

The spectral locations of the peaks also illustrate the impact of SLR on the photon-pair generation. For $\chi^{(2)}_{yyy}$, where all fields are y-polarized, only the local field at $\lambda_p = 603$ nm is enhanced by the SLR, and thus the strongest signal is generated at $\lambda = 1206$ nm. Similarly for $\chi^{(2)}_{xyx}$, only the x-polarized signal field is enhanced by the SLR, and thus the signal peak is located at $\lambda_s = 1203$ nm. As mentioned before, the process of $\chi^{(2)}_{yxx}$ utilizes SLRs at both pump and signal wavelength resulting in the strongest response of the three allowed processes. The overlap between $E_{loc,p}$ and $E_{loc,s}$ then shifts the signal peak to 1205 nm, since y-polarized SLR wavelength (603 nm) is not exactly half of the x-polarized SLR wavelength (1204 nm). This result implies, that by iteratively improving the design in order to better spectrally overlap the two SLRs, even stronger signal enhancement could be expected.

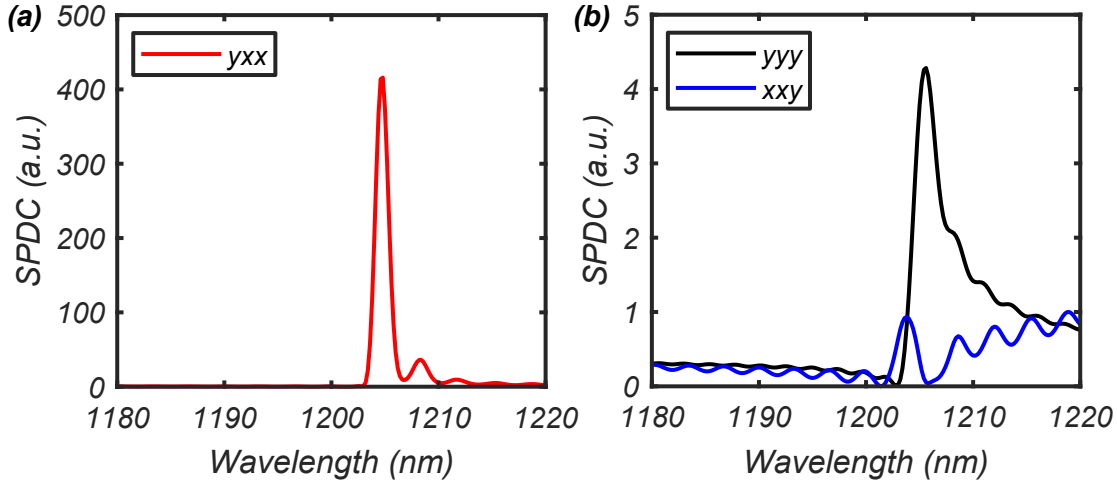

Figure 5.5. *Spontaneous parametric down-conversion (SPDC) as a function of the signal wavelength. The signals illustrated with* ***(a)*** *red,* ***(b)*** *black and blue curves correspond to processes described by the tensor components $\chi^{(2)}_{yxx}$, $\chi^{(2)}_{yyy}$, and $\chi^{(2)}_{xxy}(=\chi^{(2)}_{xyx})$, respectively. The responses are normalized to the weakest signal peak in our simulation band.*

When considering quantum optics and other applications of coherent photon pairs, our results here are quite two sided. On the other hand, the relatively narrow linewidths ($\sim$2 nm) of our signal bands illustrate the high coherence of the generated photon pairs. Furthermore, our results suggest that y-polarized illumination on our sample would result in an efficient generation of x-polarized photon pairs. Thus, the metasurface mimics a type I nonlinear crystal commonly used in quantum optics. On the other hand, however, the process corresponding to $\chi^{(2)}_{xyx}$ would be most useful for quantum optics, since it would result in the generation of an entangled photon pair with orthogonal polarizations. For this process, the multiresonant design is not beneficial but rather disadvantageous even. It would be more useful to utilize singly-resonant conditions where the SLRs enhance the signal fields for both polarizations. However, this would require other enhancement methods for the pump wavelength. As one solution, we propose utilization of a DBR cavity, which we demonstrate in the next section.

5.3 Singly-resonant Metasurface in Bragg Cavity

As the second option, we studied a singly-resonant-in-cavity (SRC) design, shown in Figure 5.6. Here, a singly-resonant metasurface, consisting of the same aluminum nanoparticles as the earlier sample design, is placed in the center of a DBR cavity. Now, the nanoparticles are arranged in a square lattice ($p_x = p_y = 793$ nm) giving a rise to a SLR at $\lambda_s = 1150$ nm for both x- and y- polarized light. The DBRs consist of ten layer pairs of titanium dioxide (TiO_2, $n = 2.5$) and silicon dioxide (SiO_2, $n = 1.45$), and they are designed to reflect light around $\lambda_B = 550$ nm.

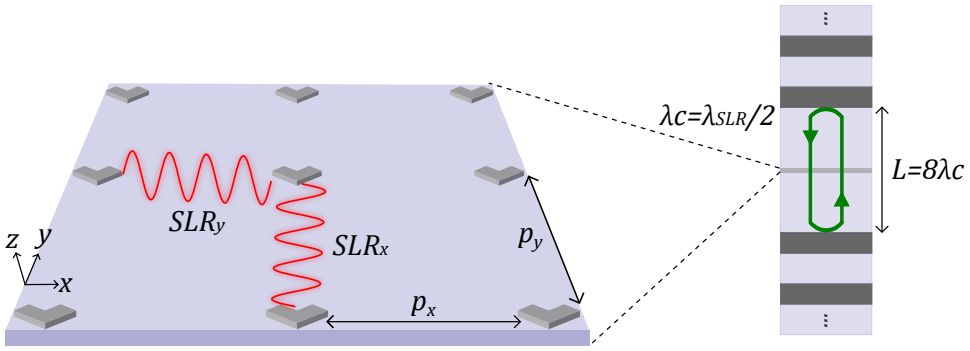

Figure 5.6. *Schematic drawing of a sample consisting of a DBR cavity and a singly-resonant metasurface. DBRs are formed with ten layer pairs of titanium dioxide (TiO_2, $n = 2.5$) and silicon dioxide (SiO_2, $n = 1.45$) and they are designed to reflect light around $\lambda_B = 550$ nm. The DBR cavity is used to enhance the field at the pump wavelength ($\lambda_c = \lambda_p = 575$ nm) and SLRs are used to enhance the local field at signal wavelength ($\lambda_{SLR} = \lambda_s = 1150$ nm).*

Unlike the typical DBR cavities, we selected our cavity wavelength $\lambda_c = \lambda_p = 575$ nm to differ from $\lambda_B = 550$ nm. This selection helped us to have lossless propagation for the generated signal and to avoid overlapping of SLR-peaks with the DBR-transmission sidebands. Therefore, we should obtain strong local field enhancements close to the metasurface using cavity coupling and SLRs at λ_p and λ_s, respectively. Since the operation of the DBR is independent of the input polarization, and SLRs have the same wavelength for x- and y-polarized light, the SRC design should give equal enhancement for all allowed second-order tensor components. In theory, SRC design could then mimic crystal types 0, I and II, which is a clear advantage over the conventional phase-matched materials. $\chi^{(2)}_{xxy} = \chi^{(2)}_{xyx}$ is especially a subject of interest since it corresponds to the process where the generated photons have orthogonal polarizations. Now, we can list relevant sample parameters and enhancement methods for the SRC sample design in Table 5.3.

Like in the previous simulations, we started by defining the linear properties with FDTD. The transmission spectrum shown in Figure 5.7 is very similar to the typical transmission spectrum of a uniform DBR (see Figure 3.3). The wide reflection region around $\lambda_B = 550$ nm and the strong sidebands (marked with black arrows in Figure 5.7) are the consequences of a relatively small number of layer pairs and the high difference between the

Table 5.3. *Metasurface parameters, the designed signal wavelength λ_s, enhancement resonances for pump and signal wavelengths, and optimal tensor components for singly-resonant-in-cavity (SRC) design. Periods p_x and p_y are the lattice constants in x- and y-coordinates, respectively.*

Sample	λ_s (nm)	p_x (nm)	p_y (nm)	pump resonance	signal resonance	tensors
SRC	1150	793	793	cavity mode	SLR_y, SLR_x	xxy, yxx, yyy

refractive indexes of TiO_2 ($n = 2.5$) and SiO_2 ($n = 1.45$). There are many methods to make the reflection band narrower and to reduce the strengths of the sidebands, but they are beyond the scope of this Thesis. Here, we are more interested in the properties of the cavity and the metasurface.

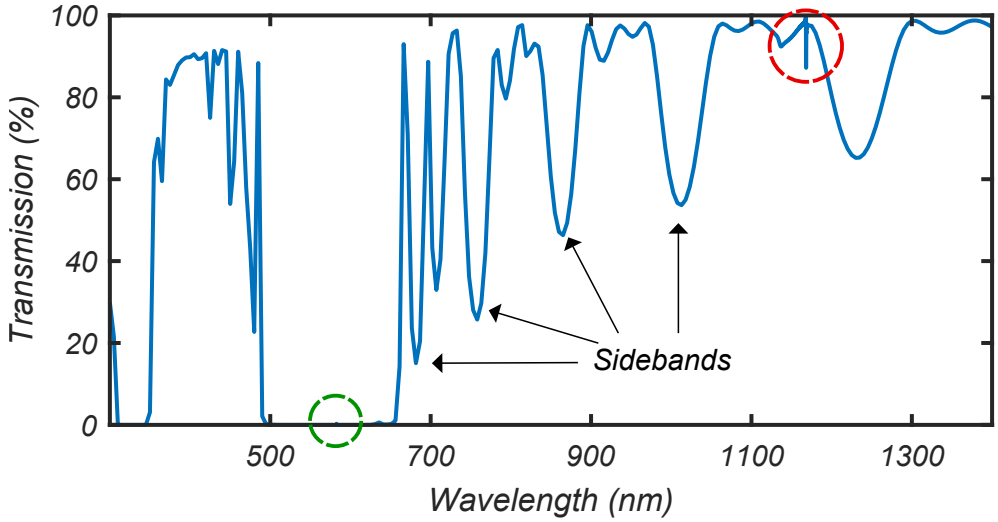

Figure 5.7. *Transmission spectrum of the SRC design. A SLR peak is detected at 1168 nm, marked with the red circle, otherwise the spectrum looks typical for a uniform DBR. Here, the sidebands typical for an uniform DBR are marked with black arrows. There is also a small transmission peak at 583 nm, marked with the green circle, but due to the scaling of the y-axis it is not visible here.*

The spectrum in Figure 5.7 shows the influences of the cavity modes and the SLR. The resonance peak for cavity mode locates at $\lambda = 583$ nm while the SLR peak is seen at $\lambda = 1168$ nm. The resonance wavelengths differ slightly from the designed values. Fortunately, they differ roughly by a factor of two, and thus we should still get the multiresonant conditions fulfilled for SPDC. Furthermore, peaks have relatively low amplitudes, and thus, they are re-plotted for clarity in Figure 5.8. We also note that the spectra for x- and y-polarized light are almost identical, as was intended. We can thus limit our visualization to the x-polarized input.

Now, we can again estimate the linewidths and Q-factors of our resonances. The cavity resonance at 583 nm has the linewidth $\Delta\lambda = 0.12$ nm and thus Q-factor of value 4850. For the SLR at 1168 nm, the corresponding values are $\Delta\lambda = 0.35$ nm and $Q = 3340$. These Q-factors are now an order-of-magnitude larger than the SLR Q-factors of the previous design. However, this is a consequence of a higher simulation resolution required

for the SRC simulations.

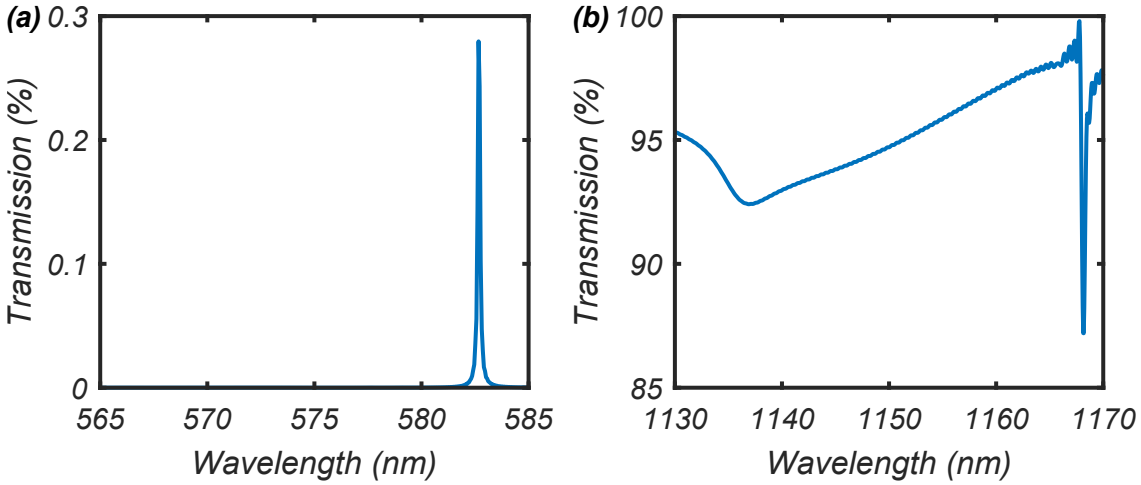

Figure 5.8. *Transmission spectrum of the SRC design close to* ***(a)*** *the pump wavelength and* ***(b)*** *signal wavelength. The cavity mode resonance is detected as a peak in the spectrum at 538 nm, and the SLR as a dip at 1168 nm.*

The next step in our study was, yet again, the evaluation of the local field profiles visualized in Figure 5.9. As was expected , the field profiles, which are again normalized to the incident field, have very narrow spectral features at the resonance wavelengths. The SLR induced enhancement is of similar strength than with multiresonant design (see Figure 5.4). Same can not be said for the local field at the cavity resonance, which is surprisingly low. This might result from slightly inaccurate simulations, which also impacts the amplitude and the Q-factor of the resonance peak. For example, the Q-factor of a FP etalon with our cavity length should be roughly ten times larger to the simulated value. Keeping this in mind, we continue our evaluation with the relevant linear properties listed in Table 5.4.

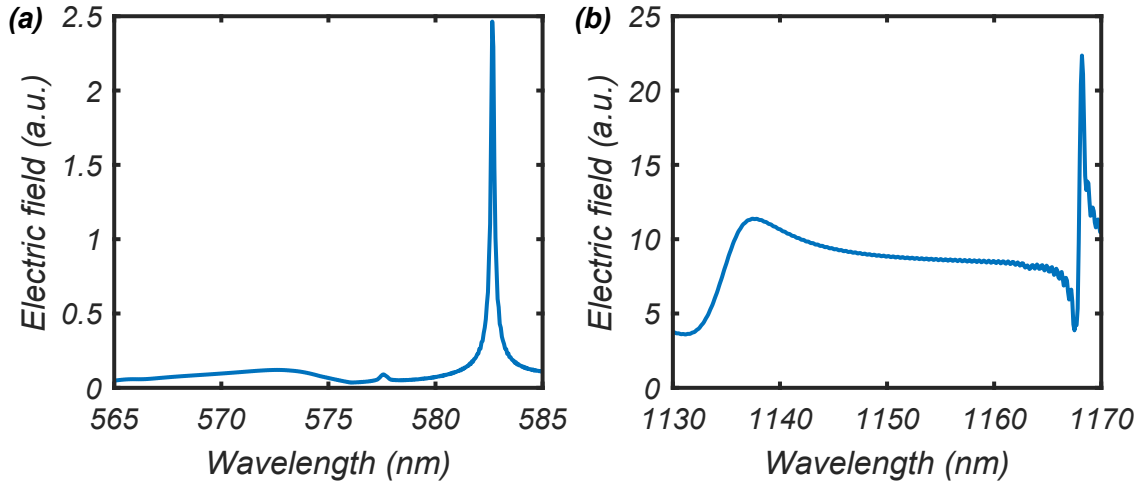

Figure 5.9. *Normalized local electric fields in the SRC design close to* ***(a)*** *the pump wavelength and* ***(b)*** *signal wavelength.*

Next, we applied NLST methodology to calculate the SPDC spectrum shown in Figure 5.10. Unlike the SPDC spectrum for the multiresonant design, there are now two dis-

Table 5.4. *Simulation results for the cavity mode resonance and SLR for the SRC design. The resonances locate at wavelengths λ, have linewidths $\Delta\lambda$, quality factors Q and the maximum local field enhancement factors E_{loc}.*

Resonance	λ (nm)	$\Delta\lambda$ (nm)	Q	E_{loc}
Cavity mode	583	0.12	4850	2.5
SLR	1168	0.35	3340	21

tinguishable and narrow peaks. The stronger peak locates at the SLR wavelength 1168 nm and the other, a slightly weaker peak at 1165 nm, which is exactly twice the cavity mode wavelength. This once again illustrates the enhancing impact of high-Q-factor resonances. The fact that there are two peaks is the consequence of the overlap integral that is being used in the NLST method to estimate the signal strength. The linewidths of the two resonance peaks are so narrow that they do not properly overlap. Thus, the signal is enhanced at two separate wavelengths instead of one. By better overlapping between these two resonances, we should have only one signal peak with a dramatically larger enhancement factor.

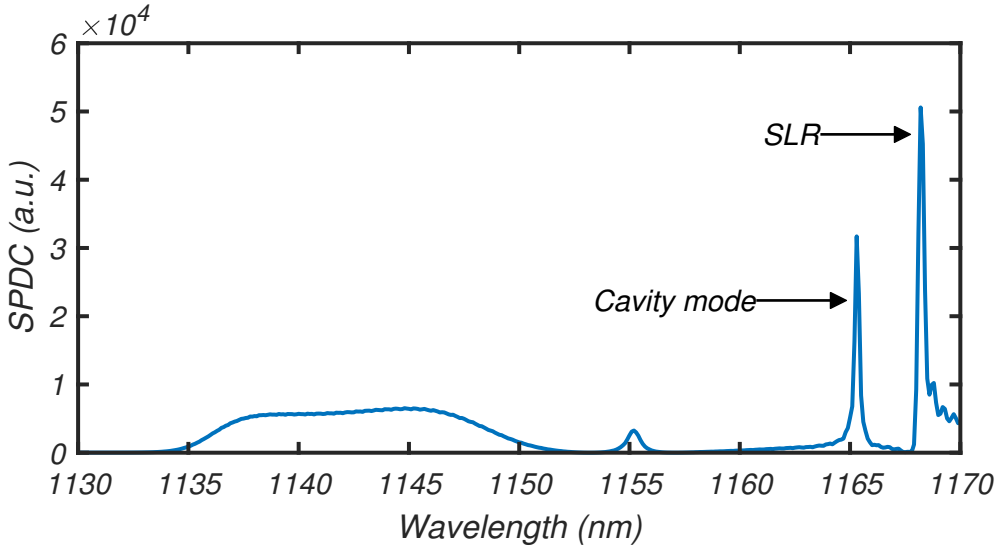

Figure 5.10. *Spontaneous parametric down-conversion spectrum of the SRC design. The emission peaks at 1165 nm and 1168 nm result from field enhancements by coupling to the cavity mode and SLR mode, respectively.*

When considering the local-field enhancements listed in Table 5.4, the two peak amplitudes are surprisingly close to each other. Especially when we recall that SLR enhances two of the relevant fields, while the cavity mode enhances only one. Here, it is worth recalling that the values listed Table 5.4 are for the single unit volume, where the field was at maximum. Moreover, the overlap integral of NLST covers the whole simulation volume. SLR indeed creates a stronger local field near the nanoparticles. However, the coupling into the cavity mode causes an equally strong field over the whole simulation volume. Therefore, the cavity mode enhancement is of the same order-of-magnitude than the SLR enhancement.

Again, it is worth to mention that the SPDC spectrum is very close to the one shown in Figure 5.10 for all allowed tensor components. Thus, we display only the results corresponding to $\chi^{(2)}_{xxy} = \chi^{(2)}_{xyx}$ (type II process) since it is the most useful for applications in quantum optics. We also note that the two other processes, corresponding to $\chi^{(2)}_{yyy}$ (type 0) and $\chi^{(2)}_{yxx}$ (type I), would be more useful for SHG. This multi-functionality, however, was designed and is the main advantage of the SRC design over the multiresonant design.

6 CONCLUSION

In this Thesis, we demonstrated how the utilization of high-quality-factor resonances improves the nonlinear optical properties of metamaterials. Here, we focused on two second-order processes: Second-harmonic generation (SHG) and spontaneous parametric down-conversion (SPDC). We successfully performed experiments that confirm the impact of high-quality-factor resonances and also validate our simulation methods. We then proceeded to design two novel plasmonic metamaterial structures that rely on two types of high-quality-factor resonances.The first resonance is a collective response of periodic structures known as surface lattice resonance (SLR) and guided-mode resonance (GMR) in plasmonic and dielectric metamaterials, respectively. The second resonance rises from the coupling of the incident light into an optical cavity.

First, we characterized linear and nonlinear optical properties of fully dielectric resonant waveguide gratings (RWGs) made of silicon nitride. We studied two RWGs with different grating periods and noticed the enhancing impact of GMRs with both samples. In the transmission spectra, we detected narrow spectral features at predicted locations with relatively high Q-factors of ~ 400. At the same spectral locations, we measured strong SH responses with up to 650-fold enhancement when compared against the off-resonance signal.

Next, we used the finite-difference time-domain (FDTD) method to simulate the linear properties of our RWGs. The simulated transmission spectra had GMR peaks close to the experimental locations with Q-factors up to 1600. With FDTD we also simulated the local fields at fundamental and SH wavelength on the grating surfaces. Then based on nonlinear scattering theory (NLST), we used the simulated field profiles to numerically evaluate SH emission from our samples. Now, the SH emission was up to 1000-fold enhanced when compared against the off-resonance values.

The proof-of-principle studies summarized above confirm two things. First, utilizing GMRs in fully dielectric materials improve their nonlinear properties. In the future, realizing the multi-resonant conditions with GMRs in RWGs could enable the enhancement of other nonlinear processes. For example, realizing cascaded third-harmonic generation could pave the way towards efficient UV light source in nanoscale. Second, the simulations agree rather well with experiments validating the chose simulation methods of FDTD and NLST to predict the nonlinear responses of metamaterials. The differences between experiments and simulations can be explained with the inaccuracies of our experimental setup. Thus, we can use the presented simulation methods to design metamaterials for

future investigations.

Next, we designed two plasmonic metamaterials for efficient SPDC. The basic building blocks for both designs were L-shaped aluminum nanoparticles surrounded by a homogeneous medium, such as glass. This particle symmetry enables three types of SPDC processes. One where pump and signal have the same polarization (type 0), one where they have orthogonal polarizations (type I), and one where the two signal photons have orthogonal polarizations (type II). The two latter processes are used in quantum optics for coherent photon-pair generation. The SPDC responses were enhanced by designing high-quality-factor resonances at both pump and signal wavelengths, i.e. by utilizing multi-resonant conditions.

The first sample design was a metasurface where the nanoparticles were arranged in a rectangle lattice. Then, the design gave rise to SLRs at the pump and signal wavelengths for orthogonal polarizations. For the SLRs, the FDTD simulations gave Q-factors of 430 and 550 at the pump and signal wavelengths, respectively. As expected, the type I process, for which the multi-resonant conditions were the most utilized, was the strongest of the three processes. It had more than 100-fold enhancement for the SPDC signal when compared against the other two processes, which enhanced only one of the relevant local fields. For all allowed processes, the SPDC signal was enhanced inside a relatively narrow wavelength band. This implies that the generated photon pairs are highly coherent, which is a significant advantage over the traditional nonlinear crystals.

For the second sample design, we placed a singly-resonant metasurface into a cavity made of two distributed Bragg reflectors. Now, the multi-resonant conditions were achieved by coupling the pump into the cavity and enhancing the local fields at the signal wavelength by using a SLR. An advantage of this configuration was that the linear response of the structure is independent of the polarization. This way, the sample design can act as type 0, type I and type II nonlinear material, depending on the input polarization. With FDTD, we simulated Q-factors of 3300 and 4800 for the SLR and the cavity mode, respectively. The SLR does not coincide exactly with the doubled cavity mode wavelength. Thus, the SPDC is enhanced at two wavelengths: At the doubled cavity mode wavelength and at the SLR wavelength. By better overlapping between these two signal peaks, we should get even more enhanced SPDC responses with extremely narrow linewidths.

Both sample designs show great potential for dramatically enhancing second-order nonlinear responses in the nanoscale. The results here encourage to fabricate the presented sample designs. For this, however, the modest initial step should be considered, since the multi-resonant conditions are highly sensitive of the input wavelength. As a start, we should realize the multi-resonant condition in a single metasurface. As a first step for the DBR-based structures, we should realize a cavity-enhanced SHG using a metasurface that utilizes a broader type of resonance, e.g. localized surface plasmon resonance or a SLR of lower Q-factor value.

We conclude this Thesis by noting that the enhancement methods and sample designs presented here are not limited to improving only SHG and SPDC. Other linear and nonlinear processes could also be investigated. Field enhancements at fundamental and SH wavelengths, which are achievable with SLRs and cavity modes alike, should also give rise to cascaded third-harmonic generation. Another example process is DFG, which could lead to efficient emission of THz waves. With these two example processes, and with numerous others, we could find novel approaches towards nonlinear applications in the nanoscale.

REFERENCES

[1] P. A. Franken, A. E. Hill, C. W. Peters, and G. Weinreich. Generation of optical harmonics. In: *Physical Review Letters* 7.4 (1961), 118–119. DOI: 10.1103/PhysRevLett.7.118.

[2] C. C. Wang and G. W. Racette. Measurement of parametric gain accompanying optical difference frequency generation. In: *Applied Physics Letters* 6.8 (1965), 169–171. DOI: 10.1063/1.1754219.

[3] R. W. Boyd. *Nonlinear optics*. 3rd. San Diego, Calif: Academic Press, 2008. ISBN: 0123694701.

[4] S. E. Harris, M. K. Oshman, and R. L. Byer. Observation of tunable optical parametric fluorescence. In: *Physical Review Letters* 18.18 (1967), 732–734. DOI: 10.1103/PhysRevLett.18.732.

[5] L. G. Helt, M. Liscidini, and J. E. Sipe. How does it scale? Comparing quantum and classical nonlinear optical processes in integrated devices. In: *Journal of the Optical Society of America B: Optical Physics* 29.8 (2012), 2199–2212. DOI: 10.1364/JOSAB.29.002199.

[6] G. Harder, T. J. Bartley, A. E. Lita, S. W. Nam, T. Gerrits, and C. Silberhorn. Single-Mode Parametric-Down-Conversion States with 50 Photons as a Source for Mesoscopic Quantum Optics. In: *Physical Review Letters* 116.14 (2015), 143601. DOI: 10.1103/PhysRevLett.116.143601.

[7] S. Lemieux, E. Giese, R. Fickler, M. V. Chekhova, and R. W. Boyd. A primary radiation standard based on quantum nonlinear optics. In: *Nature Physics* 15.6 (2019), 529–532. DOI: 10.1038/s41567-019-0447-2.

[8] G. S. He. *Nonlinear Optics and Photonics*. Oxford University Press, 2015. ISBN: 9780198702764.

[9] O. Svelto. *Principles of lasers*. 5. New York, NY: Springer, 2010. ISBN: 9781441913012.

[10] M. Decker, M. Ruther, C. E. Kriegler, J. Zhou, C. M. Soukoulis, S. Linden, and M. Wegener. Strong optical activity from twisted-cross photonic metamaterials. In: *Optics Letters* 34.16 (2009), 2501–2503.

[11] J. Kim, A. Dutta, G. V. Naik, A. J. Giles, F. J. Bezares, C. T. Ellis, J. G. Tischler, A. M. Mahmoud, H. Caglayan, O. J. Glembocki, A. V. Kildishev, J. D. Caldwell, A. Boltasseva, and N. Engheta. Role of epsilon-near-zero substrates in the optical response of plasmonic antennas. In: *Optica* 3.3 (2016), 339–346. DOI: 10.1364/OPTICA.3.000339.

[12] N. Yu, P. Genevet, M. A. Kats, F. Aieta, J.-P. Tetienne, F. Capasso, and Z. Gaburro. Light Propagation with Phase Discontinuities: Generalized Laws of Reflection and Refraction. In: *Science* 334.6054 (2011), 333–337. DOI: 10.1126/science.1210713.

[13] P. Genevet, F. Capasso, F. Aieta, M. Khorasaninejad, and R. Devlin. Recent advances in planar optics: From plasmonic to dielectric metasurfaces. In: *Optica* 4.1 (2017), 139–152. DOI: 10.1364/OPTICA.4.000139.

[14] F. Aieta, M. A. Kats, P. Genevet, and F. Capasso. Multiwavelength achromatic metasurfaces by dispersive phase compensation. In: *Science* 347.6228 (2014), 1342–1345.

[15] M. Li, J. Song, and F. Wu. Ultra-compact chiral metamaterial with negative refractive index based on miniaturized structure. In: *Journal of Magnetism and Magnetic Materials* 426 (2017), 150–154. DOI: 10.1016/j.jmmm.2016.11.066.

[16] F. Bilotti, S. Tricarico, and L. Vegni. Plasmonic Metamaterial Cloaking at Optical Frequencies. In: *IEEE Transactions on Nanotechnology* 9.1 (2010), 55–61. DOI: 10.1109/TNANO.2009.2025945.

[17] G. Li, S. Zhang, and T. Zentgraf. Nonlinear photonic metasurfaces. In: *Nature Reviews Materials* 2.5 (2017). DOI: 10.1038/natrevmats.2017.10.

[18] M. Kauranen and A. V. Zayats. Nonlinear plasmonics. In: *Nature Photonics* 6.11 (Nov. 2012), 737–748. DOI: 10.1038/nphoton.2012.244.

[19] T. Ning, H. Pietarinen, O. Hyvärinen, R. Kumar, T. Kaplas, M. Kauranen, and G. Genty. Efficient second-harmonic generation in silicon nitride resonant waveguide gratings. In: *Optics Letters* 37.20 (2012), 4269–4271. DOI: 10.1364/OL.37.004269.

[20] J. Kim, C. Kumar, M. Cha, H. Choi, K. J. Kim, and N. Peyghambarian. Quasi-phase-matched third harmonic generation in organic multilayers. In: *SCIENTIFIC REPORTS* 8.1 (2018), 1–7.

[21] S. Liu, M. B. Sinclair, S. Saravi, G. A. Keeler, Y. Yang, J. Reno, G. M. Peake, F. Setzpfandt, I. Staude, T. Pertsch, and I. Brener. Resonantly Enhanced Second-Harmonic Generation Using III-V Semiconductor All-Dielectric Metasurfaces. In: *Nano Letters* 16.9 (2016), 5426–5432.

[22] R. Czaplicki, M. Zdanowicz, K. Koskinen, H. Husu, J. Laukkanen, M. Kuittinen, and M. Kauranen. Linear and nonlinear properties of high-quality l-shaped gold nanoparticles. In: *Nonlinear Optics Quantum Optics* 45.1-2 (2012), 71–83.

[23] H. Husu, J. Mäkitalo, J. Laukkanen, M. Kuittinen, and M. Kauranen. Particle plasmon resonances in L-shaped gold nanoparticles. In: *Optics Express* 18.16 (2010). DOI: 10.1364/OE.18.016601.

[24] L. R. O. P.R.S. III. Note on the remarkable case of diffraction spectra described by Prof. Wood. In: *The London, Edinburgh, and Dublin Philosophical Magazine and Journal of Science* 14.79 (1907), 60–65. DOI: 10.1080/14786440709463661.

[25] A. A. Darweesh, S. J. Bauman, D. T. Debu, and J. B. Herzog. The Role of Rayleigh-Wood Anomalies and Surface Plasmons in Optical Enhancement for Nano-Gratings. In: *Nanomaterials (Basel, Switzerland)* 8.10 (2018), 809. DOI: 10.3390/nano8100809.

[26] R. Czaplicki, A. Kiviniemi, J. Laukkanen, J. Lehtolahti, M. Kuittinen, and M. Kauranen. Surface lattice resonances in second-harmonic generation from metasurfaces. In: *Optics letters* 41.12 (June 2016), 2684.

[27] R. Czaplicki, A. Kiviniemi, M. J. Huttunen, X. R. Zang, T. Stolt, I. Vartiainen, J. Butet, M. Kuittinen, O. Martin, and M. Kauranen. Less Is More: Enhancement of Second-Harmonic Generation from Metasurfaces by Reduced Nanoparticle Density. In: *NANO LETTERS* 18.12 (2018), 7709–7714.

[28] M. J. Huttunen, P. Rasekh, R. W. Boyd, and K. Dolgaleva. Using surface lattice resonances to engineer nonlinear optical processes in metal nanoparticle arrays. In: *Physical Review A* 97.5 (May 2018).

[29] J. C. Maxwell. *A treatise on electricity and magnetism*. Oxford: Clarendon Press, 1873.

[30] C. F. Bohren and D. R. Huffman. *Absorption and scattering of light by small particles*. New York: Wiley, 1983. ISBN: 9780471293408.

[31] E. Hecht. *Optics*. 4th. San Francisco: Addison Wesley, 2002. ISBN: 0321188780.

[32] A. S. M. Kiviniemi. *Spectral Measurements of Second-Harmonic Generated Light*. M.Sc Thesis. Tampere University of Technology, 2018.

[33] Y. R. Shen. *The Principles of Nonlinear Optics*. 1st. New York: Wiley, 1984. ISBN: 0471889989.

[34] M. Cazzanelli, F. Bianco, E. Borga, G. Pucker, M. Ghulinyan, E. Degoli, E. Luppi, V. Véniard, S. Ossicini, D. Modotto, S. Wabnitz, R. Pierobon, and L. Pavesi. Second-harmonic generation in silicon waveguides strained by silicon nitride. In: *Nature Materials* 11.2 (2012; 2011), 148–154. DOI: 10.1038/nmat3200.

[35] D. A. Kleinman. Nonlinear dielectric polarization in optical media. In: *Physical Review* 126.6 (1962), 1977–1979.

[36] S. A. Maier. *Plasmonics: Fundamentals and Applications*. 1st. New York, NY: Springer Us, 2007. ISBN: 0387331506.

[37] P. D. Maker, R. W. Terhune, M. Nisenoff, and C. M. Savage. Effects of dispersion and focusing on the production of optical harmonics. In: *Physical Review Letters* 8.1 (1962), 21–22. DOI: 10.1103/PhysRevLett.8.21.

[38] C. Couteau. Spontaneous parametric down-conversion. In: *Contemporary Physics 59(3), 291-304 (2018)* (2018). DOI: 10.1080/00107514.2018.1488463.

[39] H. D. Saleh, S. Vezzoli, L. Caspani, A. Branny, S. Kumar, B. D. Gerardot, and D. Faccio. Towards spontaneous parametric down conversion from monolayer MoS2. English. In: *Scientific Reports* 8.1 (2018), 1–7. DOI: 10.1038/s41598-018-22270-4.

[40] C. C. Gerry and P. Knight. *Introductory quantum optics*. Cambridge, UK; New York: Cambridge University Press, 2005. ISBN: 9780511648373.

[41] L.-A. Wu, H. J. Kimble, J. L. Hall, and H. Wu. Generation of squeezed states by parametric down conversion. In: *Physical Review Letters* 57.20 (1986), 2520–2523. DOI: 10.1103/PhysRevLett.57.2520.

[42] D. W. F. Graham Smith Terry A. King. *Optics and Photonics: An Introduction*. 2. Chichester, West Sussex: Wiley, 2007. ISBN: 9780470017838.

[43] R. Kashyap. *Fiber Bragg Gratings*. 2nd. US: Academic Press, 2009. ISBN: 0123725798.

[44] K. Utaka, S. Akiba, K. Sakai, and Y. Matsushima. /4-shifted InGaAsP/InP DFB lasers by simultaneous holographic exposure of positive and negative photoresists. In: *Electronics Letters* 20.24 (1984), 1008. DOI: 19840686.

[45] K. Gbele. Fabrication of novel structures to enhance the performance of microwave, millimeter wave and optical radiators. PhD thesis. 2016. ISBN: 1339-769239.

[46] M. P. Nielsen and A. Y. Elezzabi. Nanoplasmonic distributed Bragg reflector resonators for monolithic integration on a complementary metal-oxide-semiconductor platform. In: *Applied Physics Letters* 103.5 (2013), 51107. DOI: 10.1063/1.4817547.

[47] Y. M. Kang, A. Arbabi, and L. L. Goddard. A microring resonator with an integrated Bragg grating: a compact replacement for a sampled grating distributed Bragg reflector. English. In: *Optical and Quantum Electronics* 41.9 (2009), 689–697. DOI: 10.1007/s11082-010-9380-4.

[48] G. Singh, P. Purnawirman, J. D. B. Bradley, N. Li, E. S. Magden, M. Moresco, T. N. Adam, G. Leake, D. Coolbaugh, and M. R. Watts. Resonant pumped erbium-doped waveguide lasers using distributed Bragg reflector cavities. English. In: *Optics Letters* 41.6 (2016), 1189–1192.

[49] T. Erdogan. Fiber grating spectra. In: *Journal of Lightwave Technology* 15.8 (1997), 1277–1294.

[50] J. A. Giordmaine and R. C. Miller. Optical parametric oscillation in the visible spectrum. In: *Applied Physics Letters* 9.8 (1966), 298–300. DOI: 10.1063/1.1754758.

[51] M. H. Dunn and M. Ebrahimzadeh. Parametric Generation of Tunable Light from Continuous-Wave to Femtosecond Pulses. In: *Science* 286.5444 (1999), 1513–1517. DOI: 10.1126/science.286.5444.1513.

[52] D. Smirnova and Y. S. Kivshar. Multipolar nonlinear nanophotonics. In: *Optica* 3.11 (2016), 1241–1255.

[53] B. K. Canfield, S. Kujala, K. Jefimovs, J. Turunen, and M. Kauranen. Linear and nonlinear optical responses influenced by broken symmetry in an array of gold nanoparticles. In: *Optics Express* 12.22 (2004), 5418–5423. DOI: 10.1364/OPEX.12.005418.

[54] H. P. Myers. *Introductory to Solid State Physics*. Second. Taylor and Francis, 1997.

[55] E. Ringe, J. M. McMahon, K. Sohn, C. Cobley, Y. Xia, J. Huang, G. C. Schatz, L. D. Marks, and R. P. V. Duyne. Unraveling the Effects of Size, Composition, and Substrate on the Localized Surface Plasmon Resonance Frequencies of Gold and Silver Nanocubes: A Systematic Single-Particle Approach. In: *The Journal of Physical Chemistry C* 114.29 (2010), 12511–12516. DOI: 10.1021/jp104366r.

[56] D. Rosenblatt, A. Sharon, and A. A. Friesem. Resonant grating waveguide structures. In: *IEEE Journal of Quantum Electronics* 33.11 (1997), 2038–2059. DOI: 10.1109/3.641320.

[57] W. Gao, J. Shu, C. Qiu, and Q. Xu. Excitation of Plasmonic Waves in Graphene by Guided-Mode Resonances. In: *ACS Nano* 6.9 (2012), 7806–7813. DOI: 10.1021/nn301888e.

[58] J. Li, N. Verellen, and P. V. Dorpe. Engineering electric and magnetic dipole coupling in arrays of dielectric nanoparticles. In: *Journal of Applied Physics* 123.8 (2018), 83101. DOI: 10.1063/1.5018312.

[59] F.-P. Lin, H.-L. Hsu, C.-J. Chang, S.-C. Lee, and J.-K. Chen. Surface lattice resonance of line array of poly (glycidyl methacrylate) with CdS quantum dots for label-free biosensing. In: *Colloids and Surfaces B: Biointerfaces* 179 (2019), 199–207. DOI: 10.1016/j.colsurfb.2019.03.073.

[60] T. W. W. Maß and T. Taubner. Incident Angle-Tuning of Infrared Antenna Array Resonances for Molecular Sensing. In: *ACS Photonics* 2.10 (2015), 1498–1504. DOI: 10.1021/acsphotonics.5b00399.

[61] P. Atkins and R. Friedman. *Molecular quantum mechanics*. 4th. Oxford: Oxford University Press, 2005. ISBN: 0199274983.

[62] D. C. Hooper, C. Kuppe, D. Wang, W. Wang, J. Guan, T. W. Odom, and V. K. Valev. Second Harmonic Spectroscopy of Surface Lattice Resonances. In: *Nano Letters* 19.1 (2019), 165–172. DOI: 10.1021/acs.nanolett.8b03574.

[63] M. Celebrano, X. Wu, M. Baselli, S. Großmann, P. Biagioni, A. Locatelli, C. D. Angelis, G. Cerullo, R. Osellame, B. Hecht, L. Duò, F. Ciccacci, and M. Finazzi. Mode matching in multiresonant plasmonic nanoantennas for enhanced second harmonic generation. In: *Nature Nanotechnology* 10.5 (2015; 2014), 412–417. DOI: 10.1038/nnano.2015.69.

[64] M. J. Huttunen, O. Reshef, T. Stolt, K. Dolgaleva, R. W. Boyd, and M. Kauranen. Efficient nonlinear metasurfaces by using multiresonant high-Q plasmonic arrays. In: *Journal of the Optical Society of America B* 36.7 (2019), E30. DOI: 10.1364/JOSAB.36.000E30.

[65] K. O'Brien, H. Suchowski, J. Rho, A. Salandrino, B. Kante, X. Yin, and X. Zhang. Predicting nonlinear properties of metamaterials from the linear response. In: *Nature Materials* 14.4 (2015), 379–383. DOI: 10.1038/nmat4214.

[66] J. Butet and O. J. F. Martin. Evaluation of the nonlinear response of plasmonic metasurfaces: Miller's rule, nonlinear effective susceptibility method, and full-wave computation. In: *Journal of the Optical Society of America B* 33.2 (2016), A8.

[67] S. Roke, M. Bonn, and A. V. Petukhov. Nonlinear optical scattering: The concept of effective susceptibility. In: *Physical review.B, Condensed matter and materials physics* 70.11 (2004). DOI: 10.1103/PhysRevB.70.115106.

[68] Micro and Nano Fabrication: Tools and Processes Hans H. Gatzen, Volker Saile, and Jürg Leuthold: Springer, 2015 519 pages, $99.00 (e-book 69.99) ISBN 978-3-662-44394-1. In: *MRS Bulletin* 40.10 (2015), 881. DOI: 10.1557/mrs.2015.253.

[69] D. M. Sullivan. *Electromagnetic Simulation Using the FDTD Method*. Vol. 5. John Wiley Sons, 2000. ISBN: 9781118459393.